

1 De-risking the energy transition by quantifying the uncertainties in fault stability
2 David Healy¹ & Stephen P. Hicks²
3 ¹School of Geosciences, University of Aberdeen, Aberdeen AB24 3UE United Kingdom
4 ²Department of Earth Science and Engineering, Imperial College, London SW7 2AZ United Kingdom
5 d.healy@abdn.ac.uk
6
7 This preprint is a non-peer reviewed preprint submitted to EarthArXiv.

8 De-risking the energy transition by quantifying the uncertainties in fault stability

9 David Healy¹ & Stephen P. Hicks²

10 ¹School of Geosciences, University of Aberdeen, Aberdeen AB24 3UE United Kingdom

11 ²Department of Earth Science and Engineering, Imperial College, London SW7 2AZ United Kingdom

12 d.healy@abdn.ac.uk

14 Abstract

15 The operations needed to decarbonise our energy systems increasingly involve faulted rocks in the
16 subsurface. To manage the technical challenges presented by these rocks and the justifiable public concern
17 over induced seismicity, we need to assess the risks. Widely used measures for fault stability, including slip
18 and dilation tendency and fracture susceptibility, can be combined with Response Surface Methodology from
19 engineering and Monte Carlo simulations to produce statistically viable ensembles for the analysis of
20 probability. In this paper, we describe the implementation of this approach using custom-built open source
21 Python code (*pfs* – probability of fault slip). The technique is then illustrated using two synthetic datasets and
22 two case studies drawn from active or potential sites for geothermal energy in the UK, and discussed in the
23 light of induced seismicity focal mechanisms. The analysis of probability highlights key gaps in our knowledge
24 of the stress field, fluid pressures and rock properties. Scope exists to develop, integrate and exploit citizen
25 science projects to generate more and better data, and simultaneously include the public in the necessary
26 discussions about hazard and risk.

27

28 Introduction

29 *Rationale & Objectives*

30 Faults in the crust slip in response to changes in stress or pore fluid pressure, and the source of these changes
31 can be either natural or anthropogenic. Estimating the likelihood of slip on a particular fault for a given
32 change in loading is critical for the industrial operations of the energy transition, especially geothermal
33 energy and carbon sequestration and storage (CCS). The target formations of these operations are nearly
34 always faulted and fractured to some degree, and experience from waste-water injection in the USA shows
35 how even small changes in pore fluid pressure can trigger frequent seismic slip on these faults, with
36 significant and widespread impact on society (e.g., Elsworth et al., 2016; Hincks et al., 2018; Hennings et al.,
37 2019).

38 Stephenson et al. (2019) have shown how quantitative analysis of the subsurface is one of the key
39 contributions that geoscientists can make to decarbonising energy production to meet national and
40 international targets (e.g., CCC, 2019; IPCC, 2018). This includes the systematic geomechanical
41 characterisation of rock formations, better understanding of fluid flow in fractured rocks, and the need for
42 pilot projects to explore the scaling of behaviours from the laboratory to the field. Perhaps the most
43 important aspect is to understand the public attitudes to subsurface decarbonisation technology
44 (Stephenson et al., 2019; Roberts et al., 2021). Several recent studies have addressed the uncertainties in
45 subsurface structural analysis of faulted rocks (Bond, 2015; Alcalde et al., 2017; Miocic et al., 2019). In this
46 paper, we extend this work to specifically include fault stability, and argue that in order to simultaneously
47 address public concerns and assess the viability of different schemes, we need a more rigorous approach to
48 risking subsurface decarbonisation activities, especially where these involve changes in load on faulted rocks.

49 Useful measures of fault stability include slip and dilation tendency (T_s and T_d respectively) and fracture
50 susceptibility (S_f , the change in fluid pressure to push effective stress to failure). These measures are defined
51 as functions of the *in situ* stress, the orientation of the fault plane and, in the case of S_f , rock properties. It is
52 widely recognised that the inputs for the prediction of stability are always uncertain, and to varying degrees:
53 e.g., the vertical stress component of the *in situ* stress tensor can often be quite well constrained (to within

54 5%) from density log data, whereas the maximum horizontal stress is generally much harder to quantify. To
55 improve and focus our predictions of fault stability in the subsurface, we need to accept and incorporate
56 these uncertainties into our calculations. In this paper, we describe and explore a statistical approach to fault
57 stability calculations, and then apply these methods to examples in geothermal energy, in both low- and
58 high-enthalpy settings.

59 The specific aims of this paper are to:

- 60 1. describe and explain the Response Surface Methodology, and show how it can be applied to the
61 probabilistic estimation of fault stability using a range of different measures;
- 62 2. explore how the main variables – in situ stress, fault orientation and rock properties – relate to the different
63 measures of fault stability (T_s , T_d and S_f) using synthetic (i.e., artificial) data;
- 64 3. use case studies of active and proposed geothermal projects with publicly available data to illustrate the
65 method, and then highlight the relationships between our known but uncertain input data and the predicted
66 risk of fault slip.

67 *Importance & Previous work*

68 Small changes in stress or fluid pressure (e.g., a few MPa) from human activities can have significant
69 consequences for fault stability. For example, waste-water injection from hydraulic fracturing (“fracking”)
70 operations has led to dramatic increases in seismicity in Oklahoma since 2009 (Hincks et al., 2018) and in
71 Texas since 2008 (Hennings et al., 2019; Hicks et al., 2021). The precise mechanical cause(s) of this seismicity
72 is the subject of some debate, and could be due to either ‘direct’ pore fluid pressure transfer to basement-
73 hosted faults leading to a reduction in effective stress, or ‘indirect’ poroelastic effects at a distance (Elsworth
74 et al., 2016; Goebel et al., 2019). The concept of critically stressed faults in the crust (Townend & Zoback,
75 2000), where relatively high permeability serves to maintain near-hydrostatic pore pressures, is consistent
76 with the idea that only minor perturbations in loading can have dramatic consequences, even in areas of
77 apparently low seismicity and, implicitly, low background tectonic loading.

78 In densely populated areas such as the UK, public support for, and confidence in, subsurface operations are
79 key. Hydraulic fracturing operations for shale gas in Lancashire (UK) were stopped after earthquakes were
80 triggered by fluid injection (Clarke et al., 2019). Triggered felt seismicity has already been reported at the
81 United Downs deep geothermal pilot in Cornwall (Holmgren & Werner, 2021). Note that, in both of these
82 cases, fracturing and/or fault slip are intrinsic to the success of the operation as they are needed to enhance
83 fluid flow, and therefore earthquakes are inevitable. In detail, microseismicity (i.e., $M < 2$) is inevitable, but it
84 is important to understand whether felt (i.e. $M > 2$) seismicity can be forecast ahead of time. Furthermore,
85 many sites for energy transition projects in the UK are located in (beneath) areas of extreme poverty and
86 social deprivation, both rural (e.g., Cornwall, South Wales) and urban (e.g., Greater Manchester, Glasgow),
87 and therefore the risks from these projects fall disproportionately on the less well off (Nolan, 2016;
88 McLennan et al., 2019). To begin to address these complex issues, we need to quantify which faults are more
89 or less likely to slip in response to induced changes in loading. One approach is to analyse data during
90 subsurface operations and attempt to manage the consequences (e.g., Verdon & Budge, 2018). An
91 alternative approach, and the one taken in this paper, is to look at the bigger picture before operations
92 commence and reduce risk from the outset.

93 Various measures have been proposed to quantify the propensity or tendency of a given fault to slip (or
94 open) in a known stress field. The following methods are based around an assumption of Mohr-Coulomb
95 (brittle-plastic) failure which has been shown to capture the key aspects of faulting in the upper crust. Slip
96 tendency (T_s) was introduced by Morris et al. (1996) and is the simplest measure of fault stability, defined as:

$$97 \quad T_s = \tau / \sigma_n \quad (1)$$

98 where τ is the shear stress and σ_n is the normal stress acting on the fault plane. These stress components in
99 turn depend on the principal stresses and the orientation of the fault plane (see Lisle & Srivastava, 2004 for
100 details). In the absence of cohesion, if the slip tendency on a fault equals or exceeds the coefficient of sliding
101 friction, then the fault can be deemed “unstable”. This dimensionless index embodies the key mechanical

102 principle underlying Mohr-Coulomb shear failure: as the shear (“sliding”) stress acting on a fault plane rises
 103 in relation to the normal (or “clamping”) stress, the fault approaches failure and will slip. Dilation tendency
 104 (T_d) has been defined to describe the propensity for a fault to open, or dilate, in a given stress regime:

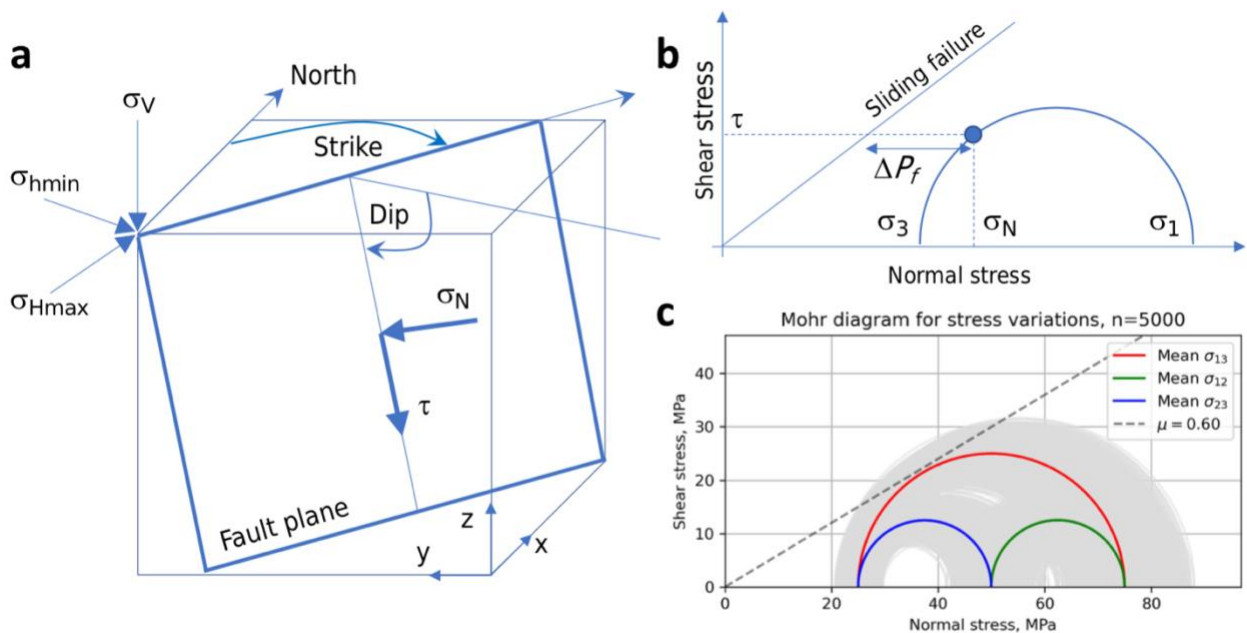
$$105 \quad T_d = (\sigma_1 - \sigma_n) / (\sigma_1 - \sigma_3) \quad (2)$$

106 where σ_1 and σ_3 are the principal stresses of the *in situ* stress tensor (Ferrill et al., 1999).

107 Most rocks in the upper crust are porous and permeable to some degree, and fault rocks are no exception,
 108 so these rocks are generally fluid saturated. This implies that we should include pore fluid pressure and the
 109 concept of effective stress in our assessment of fault stability. Fracture susceptibility (S_f) is the change in pore
 110 fluid pressure needed to push a stressed fault to failure (Streit & Hillis, 2004) and is defined by:

$$111 \quad S_f = \Delta P_f = (\sigma_n - P_f) - (\tau - C_0) / \mu \quad (3)$$

112 where P_f is the pore fluid pressure at the fault, C_0 is the cohesive strength (or cohesion), and μ is the
 113 coefficient of sliding friction (see Figure 1b).



114
 115 **Figure 1. a.** Schematic block diagram of a fault plane showing the terminology used in this paper. Also shown
 116 are the cartesian and geographic reference frames and the Andersonian principal stresses. **b.** Mohr diagram
 117 for a given state of stress (blue semi-circle) with normal (σ_n) and shear stresses (τ) marked for a selected fault
 118 plane orientation (blue dot). Failure envelope for frictional sliding (cohesion=0) also shown as straight blue
 119 line. **c.** Mohr diagram depicting one of the key issues tackled in this paper: given uncertainty in the input
 120 stress values (grey Mohr circles for the variation around the average principal stresses in red, blue and green),
 121 what is the probability of failure? i.e., what percentage of all these stress states will intersect the failure
 122 envelope?

123 Previous applications of these three measures of fault stability – T_s , T_d and S_f – cover the full spectrum of rock
 124 types and stress fields, from basins to basement and from extensional, contractional and wrench tectonic
 125 settings. Applications within the domain of the energy transition include examples from geothermal energy
 126 (both shallow and deep) and CCS. The original definition of fracture susceptibility by Streit & Hillis (2004) was
 127 concerned with safe injection limits for CO₂ in potential reservoirs in Australia. Moeck et al. (2009) used slip
 128 tendency to quantify the relative stability of different fault sets in different horizons in a geothermal reservoir
 129 in the North German Basin, and Barcelona et al. (2019) used a similar method for Copahue geothermal
 130 reservoir in Argentina. For CCS, Williams et al., (2016, 2018) have used slip tendency analyses of faults in
 131 potential sandstone reservoirs on the UK continental shelf, including the North Sea and East Irish Sea basins.
 132 The links between subsurface fluid flow, seismicity, and fault stability have recently been explored by Das &

133 Mallik (2020) for the Koyna earthquakes in India, and by Wang et al. (2020) for strike-slip faults in the Tarim
 134 Basin of China.

135 Probabilistic approaches to fault stability have been adopted by various workers. In risking CO₂ storage for
 136 an oil reservoir in the Williston basin, Ayash et al. (2009) used a features, events and processes (FEP)
 137 approach to constrain the likelihood of occurrence of fault slip (based on slip tendency) and the severity of
 138 the consequences, with their product defined as the risk. Rohmer & Bouc (2010) used RSM to assess cap rock
 139 integrity for tensile or shear failure above deep aquifers in the Paris basin targeted for the storage of CO₂.
 140 Coupled RSM and Monte Carlo approaches to fault stability have been used by Chiaramonte et al. (2008) and
 141 Walsh & Zoback (2016), following their initial application in the field of wellbore stability by Moos et al.
 142 (2003). This Fault Slip Potential (FSP) method developed by Stanford (e.g., Chiaramonte et al., 2008 & Walsh
 143 & Zoback, 2016) calculates the response surface for fracture susceptibility, with the in situ stress tensor
 144 calculated by inversion of abundant seismicity data (focal mechanisms), and then uses a Monte Carlo
 145 simulation to generate cumulative distribution functions (CDFs) of conditional probability of slip defined with
 146 reference to an arbitrary pore pressure perturbation ($\Delta P_f = 2$ MPa, in the case of Walsh & Zoback, 2016).
 147 Note that FSP assumes cohesionless faults ($C_0=0$) and hydrostatic pore fluid pressure, and that *conditional*
 148 probability in this sense refers to the fact that we do not know where any particular fault is with respect to
 149 the seismic cycle.

150 *Conventions and layout for this paper*

151 In the sections below, we describe the underlying equations for measuring fault stability and then show how
 152 we can use Response Surface Methodology (RSM) from engineering to explore the consequences of
 153 uncertainties in the input variables. After assessing the quality of the solutions obtained from RSM, we then
 154 apply a brute force Monte Carlo (MC) approach to generate cumulative distribution functions (CDFs) of the
 155 different measures (T_s , T_d and S_f). The case studies use published, publicly available data to constrain the
 156 input variable distributions and then a combined RSM/MC approach is used to explore the uncertainty in
 157 fault stability in different settings.

158 In this paper, compressive stress is reckoned positive, with σ_1 as the maximum compressive principal stress
 159 and σ_3 as the minimum principal stress. Stress states and fault regimes are assumed to be Andersonian, with
 160 one principal stress vertical, although the underlying model and code could be changed to incorporate non-
 161 Andersonian stress states with the addition of extra variables for the stress tensor orientation (Walsh &
 162 Zoback, 2016). The likelihood of slip on a fault is assessed in the framework of Mohr-Coulomb failure, with
 163 or without cohesion (Jaeger et al., 2009). Fault orientations are quantified as strike and dip, following the
 164 right-hand rule: with your right hand flat on the fault plane and fingers pointing down dip, the right thumb
 165 points in the direction (azimuth) of strike. The relationship between the geographical and cartesian reference
 166 frames follows a North-East-Down convention. Figure 1 depicts the key terms and elements used in the
 167 analysis, and Table 1 contains a list of terms and symbols used with units where appropriate.

Quantity	Symbol	Units
Maximum compressive stress	σ_1	MPa
Intermediate compressive stress	σ_2	MPa
Minimum compressive stress	σ_3	MPa
Vertical stress	σ_v	MPa
Maximum horizontal stress	σ_{Hmax}	MPa
Minimum horizontal stress	σ_{Hmin}	MPa
Azimuth of max. horizontal stress	$sHaz$	°
Pore fluid pressure	P_f	MPa
Coefficient of friction	μ	dimensionless
Cohesive strength (or cohesion)	C_0	MPa
Slip tendency	T_s	dimensionless
Dilation tendency	T_d	dimensionless
Fracture susceptibility	S_f	MPa
Fault strike	φ	°

Fault dip	δ	°
Shear stress on a fault plane	τ	MPa
Normal stress on a fault plane	σ_n	MPa

168

169 **Table 1.** List of terms and symbols used in this paper, with units where appropriate.

170

171 **Statistical analysis of geomechanical fault stability**

172 *Introduction to Response Surface Methodology (RSM)*

173 RSM is widely used in engineering and industry along with a Design of Experiments approach, and often
 174 employed to optimise a specific process of interest – e.g., to maximise the yield of a reaction given the input
 175 variables of pressure, temperature, reactant mass etc. RSM is a large and growing field and is best considered
 176 as a toolbox of different methods with a common mathematical basis. The governing equations for RSM were
 177 derived by Box & Wilson (1951). The core idea is that a response y can be represented by a polynomial
 178 function of a number (q) of input variables $x_1 - x_q$:

179
$$y = f(x_1, x_2, \dots, x_q) \quad (4)$$

180 Each of the q input variables can be represented by either a discrete set of measurements made in the
 181 laboratory (or field) or drawn from appropriate statistical distributions (normal/Gaussian, skewed normal,
 182 Von Mises etc.). The simplest polynomial function that relates y and x is a linear one:

183
$$y_i = \beta_0 + \beta_1 x_{i1} + \beta_2 x_{i2} + \dots + \beta_q x_{iq} + \epsilon_i \quad (5)$$

184
$$y_i = \beta_0 + \sum_{j=1}^q \beta_j x_{ij} + \epsilon_i \quad (6)$$

185 where β_q are the coefficients (to be determined), y_i is the set of observations of the response ($i = 1, 2, \dots, N$),
 186 and x_{ij} are the input variables ($j = 1, 2, \dots, q$). ϵ is the experimental error, and the number of ‘observations’ N
 187 $> q$, the number of input variables. This is therefore a multiple regression model linking the response y to
 188 more than one (i.e., multiple) independent variables, x .

189 A more complex polynomial relationship is the quadratic form:

190
$$y = \beta_0 + \sum_{j=1}^q \beta_j x_j + \sum_{j=1}^q \beta_{jj} x_j^2 + \sum_{i < j}^q \beta_{ij} x_i x_j + \epsilon \quad (7)$$

191 This 2nd order multiple regression model contains all the terms of the linear (1st order) model, but also extra
 192 terms for the squares and cross-products of the input variables (second and third terms on the RHS of
 193 equation 7).

194 To define a response surface, either linear or quadratic, we need to calculate the values of the β_q coefficients.
 195 We can rewrite the key equations in matrix form:

196
$$\mathbf{y} = \mathbf{X}\boldsymbol{\beta} + \boldsymbol{\epsilon} \quad (8)$$

197 where \mathbf{y} is an ($N \times 1$) vector of observations (or calculations), \mathbf{X} is an ($N \times k$) matrix of input variable values (k
 198 $= q + 1$), and $\boldsymbol{\beta}$ is a ($k \times 1$) vector of regression coefficients. We solve this system of equations using the
 199 standard linear algebra technique of least squares regression (Myers et al., 2016):

200
$$\hat{\boldsymbol{\beta}} = (\mathbf{X}'\mathbf{X})^{-1}\mathbf{X}'\mathbf{y} \quad (9)$$

201 The response surface (linear or quadratic) is then defined by

202
$$\hat{y} = \mathbf{X}\hat{\boldsymbol{\beta}} \quad (10)$$

203 The values used in \mathbf{X} are chosen to efficiently span the parameter space. A typical sampling design for \mathbf{X} is
 204 called the 3^q model with 3 values of each variable, usually the minimum, mean (or mode) and maximum. For
 205 slip tendency, $q = 6$ and this means we use $3^q = 3^6 = 729$ data points to calculate the response surface. In

206 practice, coded variables are used in \mathbf{X} where the absolute values for the minimum, mean and maximum of
 207 each variable are scaled to -1 , 0 and $+1$ respectively, and then scaled back when the response surface is used
 208 in the Monte Carlo simulation (Myers et al., 2016).

209 The response surface – i.e., the set of β coefficients – is defined using a limited number of sample points,
 210 depending on the chosen sample design (3^q in the examples used in this paper; other variants exist – see
 211 Myers et al., 2016 for details). To explore the possible variations of a response more fully, we use a Monte
 212 Carlo (MC) approach of pre-defined size ($N_{MC} = 5,000$ in the examples in this paper). The MC simulation uses
 213 the response surface calculated from the design points to calculate the responses for N_{MC} combinations of
 214 input variables drawn from their distributions. This produces a statistically viable ensemble of response
 215 values from which we can infer the probability of the response with respect to a chosen threshold.

216 With respect to fault stability, we can use RSM to produce a parameterised relationship – the response
 217 surface in q dimensions – between a stability measure of interest and the q input variables. In the case of slip
 218 tendency T_s , we can rewrite the components of equation 1 in terms of the measurable input quantities as
 219 follows:

$$220 \quad \tau = \sqrt{(\sigma_1 - \sigma_2)^2 l^2 m^2 + (\sigma_2 - \sigma_3)^2 m^2 n^2 + (\sigma_3 - \sigma_1)^2 l^2 n^2} \quad (11)$$

$$221 \quad \sigma_n = \sigma_1 l^2 + \sigma_2 m^2 + \sigma_3 n^2 \quad (12)$$

222 where l , m and n are the direction cosines of the normal (pole) to the fault plane given by

$$223 \quad l = \sin \delta \sin \phi \quad (13a)$$

$$224 \quad m = -\sin \delta \cos \phi \quad (13b)$$

$$225 \quad n = \cos \delta \quad (13c)$$

226 where ϕ is the fault strike and δ is the fault dip, in a North-East-Down reference frame (Allmendinger et al.,
 227 2012).

228 All terms on the right-hand sides of equations 11-13 are uncertain to some degree, therefore estimating the
 229 uncertainty of T_s , and as importantly, the *key controls on the uncertainty of T_s* , in terms of these input
 230 variables, is non-trivial. This difficulty in estimating and visualising possible variations in our estimates of T_s
 231 is exacerbated by the recognition that each of the input variables may be distributed differently: some
 232 quantities (e.g., the principal stresses) may follow normal (Gaussian) statistics, whereas others (e.g., strike,
 233 dip, sHmax azimuth) will follow Von Mises distributions. In the case of fracture susceptibility (S_f , equation 3),
 234 it is even more complicated with the addition of three further input variables for friction, cohesion and pore
 235 fluid pressure. Measurements or calculations of coefficients of friction and cohesive strength often display
 236 asymmetric or skewed distributions (skewed high or low), and this adds further complexity to the task of
 237 estimating and constraining fault stability from the data at hand.

238 *Worked Example 1: Slip tendency from synthetic input data*

239 The calculations presented in this paper were all performed with the custom pfs (**p**robability of **f**ault **s**lip)
 240 package, written by the first author (DH) in Python 3, and freely available on GitHub (see Code Availability,
 241 below).

242 The first example calculates a response surface for slip tendency (T_s) from $q=6$ input variables: the
 243 magnitudes of the three principal stresses of the *in situ* stress tensor (σ_1 , σ_2 , σ_3) assumed Andersonian with
 244 one principal stress vertical, the azimuth of the maximum horizontal stress (*sHaz*), and the strike and dip of
 245 the fault plane. This response surface is then used in a Monte Carlo simulation ($N_{MC} = 5,000$) to generate a
 246 CDF of T_s values for the fault. The specific Python code to run this example in the pfs package is wrapped in
 247 a Jupyter notebook available on GitHub (WorkedExample1.ipynb).

248 The first task is to define the distributions of the input variables. In pfs, examples are shown for normal,
 249 skewed normal and Von Mises (circular normal) distributions, but other statistical distributions are allowed.
 250 Table 2 and Figure 2 describe the ranges and moments of these distributions for each input variable. For this

251 example, the normally distributed principal stresses are defined with a variation (standard deviation) of 5%
 252 of their central (mean) value, and the Von Mises distributions of the azimuthal variables (sHaz, strike and dip)
 253 all have $\kappa = 200$ to model their dispersion about their mean. The fault of interest strikes 060° and dips 60° to
 254 the south (right hand rule). The key questions to be addressed by this example are:

- 255 1. given these uncertainties in the input stresses and orientation data, how does the estimation of T_s
 256 vary? What is the range and the mode?
- 257 2. which variables exert the greatest (and least) control on the predicted variation in T_s ?

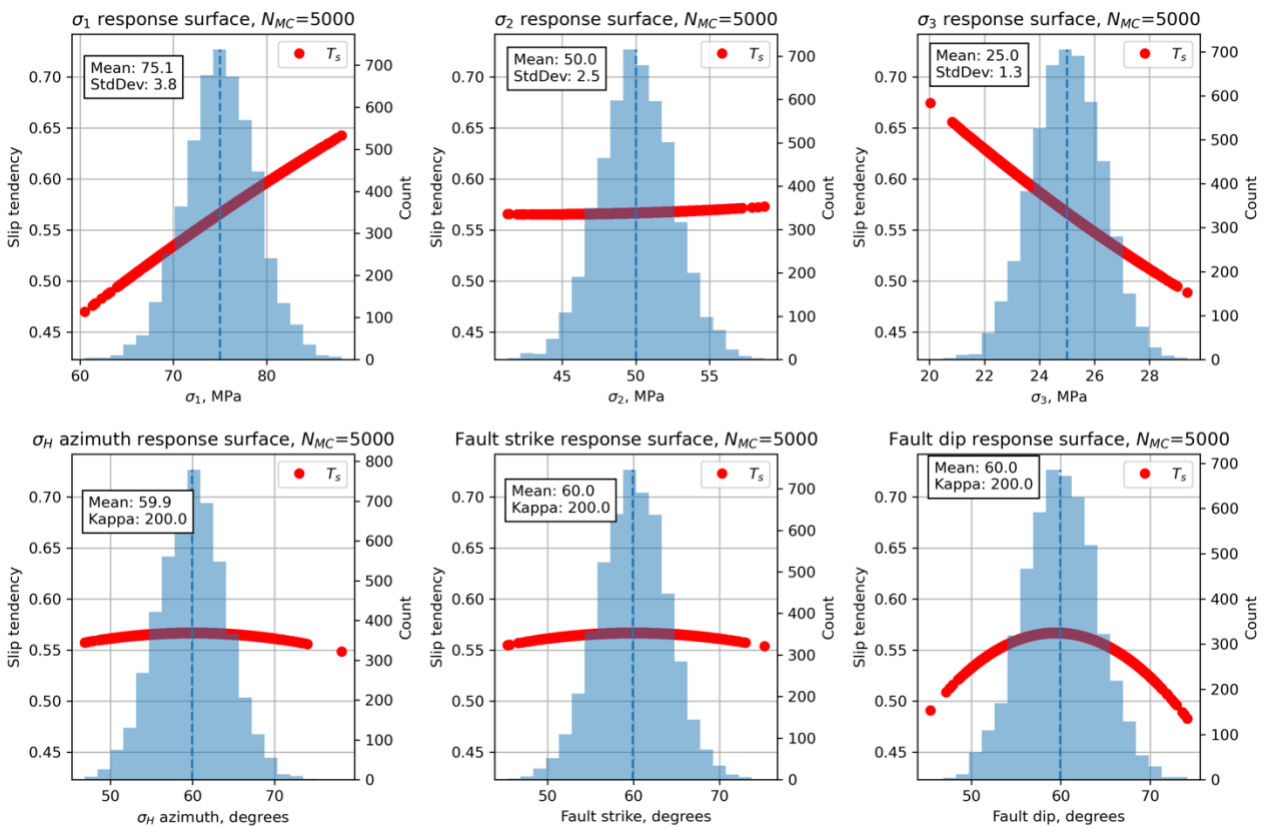
258 We first build a response surface using a 3^q design, i.e., 3 data points for each variable – minimum, mean and
 259 maximum – and for T_s , $q = 6$. This means we calculate the response surface from $3^6 = 729$ data points. We
 260 compare a calculated linear response surface with a quadratic response surface, using a normal probability
 261 plot of residuals (Figure 3). These residuals are the differences between the values of T_s derived from the
 262 observations (taken from the input distributions shown in Table 2 (upper) and Figure 2), and the calculated
 263 values of T_s using the β coefficients derived by least squares regression i.e., the response surface. The
 264 adjusted R^2 value for the quadratic 2nd order model is significantly better than that for a linear 1st order model,
 265 and we use quadratic models throughout the rest of this paper. More detailed inspection of the quality of fit
 266 between the response surface and the observations is possible, including analysis of variance, main effects
 267 plots and the use of t-statistics for each input variable to quantify their significance to the definition of the β
 268 coefficients (Myers et al., 2016). In practice, visualising sections of the response surface for individual
 269 variables is generally sufficient (see below; Moos et al., 2003; Walsh & Zoback, 2016).

Variable	Mean	Standard deviation (κ for Von Mises)	Units	Distribution	Comments
Worked Example 1 – Synthetic T_s – modelled depth=3 km					
σ_v , vertical stress	75.0	3.75 (5% of mean)	MPa	Normal	Lithostatic for depth of 3 km, assuming average rock density of 2500 kg m ⁻³
σ_H , max. horizontal stress	50.0	2.5 (5% of mean)	MPa	Normal	Andersonian normal faulting regime
σ_h , min. horizontal stress	25.0	1.25 (5% of mean)	MPa	Normal	
Azimuth of σ_{Hmax}	060	$\kappa=200$	°	Von Mises (circular Normal)	
Fault strike	060	$\kappa=200$	°	Von Mises (circular Normal)	
Fault dip	60.0	$\kappa=200$	°	Von Mises (circular Normal), truncated at 0 and 90	
Worked Example 2 – Synthetic S_f – modelled depth=3 km					
σ_v , vertical stress	75.0	7.5 (10% of mean)	MPa	Normal	Lithostatic for depth of 3 km, assuming average rock density of 2500 kg m ⁻³
σ_H , max. horizontal stress	55.0	5.5 (10% of mean)	MPa	Normal	
σ_h , min. horizontal stress	35.0	3.5 (10% of mean)	MPa	Normal	

P_f , pore fluid pressure	30.0	3.0 (10% of mean)	MPa	Normal	Hydrostatic for depth of 3 km, assuming fluid density=1000 kg m ⁻³
Azimuth of σ_{Hmax}	060	$\kappa=200$	°	Von Mises (circular Normal)	
Fault strike	060	$\kappa=200$	°	Von Mises (circular Normal)	
Fault dip	60.0	$\kappa=200$	°	Von Mises (circular Normal), truncated at 0 and 90	
Friction, μ	0.6	0.12 (20% of mean)	n/a	Skewed normal	$\alpha = -3$ i.e., skewed low
Cohesion, C_0	20.0	2.0 (10% of mean)	MPa	Skewed normal	$\alpha = +3$ i.e., skewed high

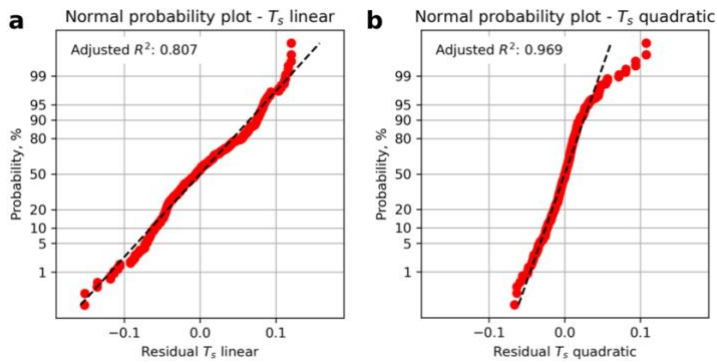
270

271 **Table 2.** Table of input variable distributions for the synthetic models in Worked Examples 1 and 2.



272

273 **Figure 2.** Histograms of input variables used to calculate slip tendency T_s for the synthetic distributions shown
274 in Table 2.



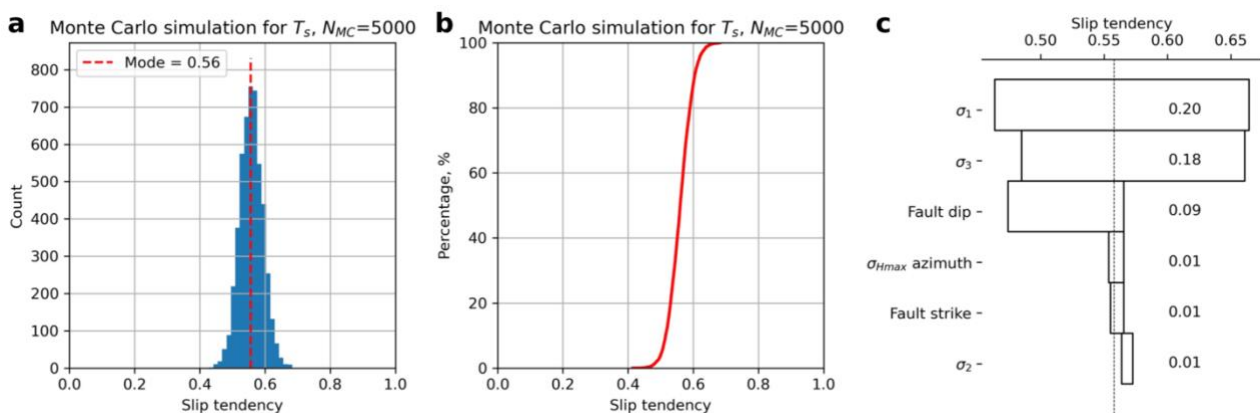
275

276 **Figure 3.** Residual plots for linear and quadratic response surfaces for slip tendency using synthetic data. The
 277 quadratic fit has a higher value of the adjusted R^2 parameter and is therefore deemed better in this case.

278 Having generated the quadratic response surface for T_s for these input distributions, we can now use it to
 279 perform a Monte Carlo (MC) simulation with the aim of generating a statistically viable ensemble from which
 280 we can infer the probability of T_s exceeding a critical value of sliding friction. The results from the MC analysis
 281 of T_s are shown in Figure 4. The histogram of all values of T_s shows a symmetrical and rather narrow
 282 distribution with a modal value of about 0.56 (Figure 4a). The CDF of all values of T_s also shows this narrow
 283 and symmetrical distribution (Figure 4b).

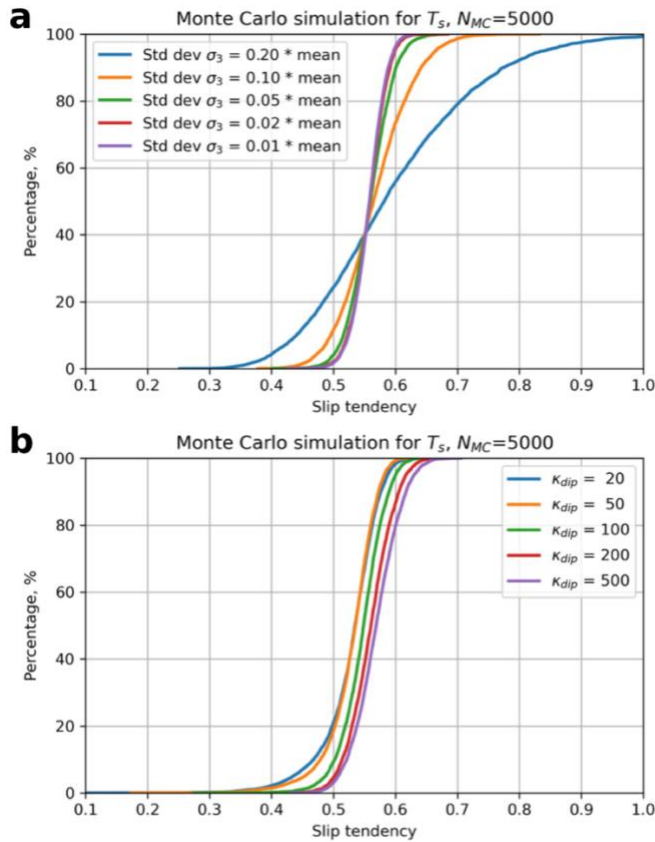
284 A response surface of more than two variables is not easy to visualise. One approach is to take sections
 285 through the surface at specific values of all but one variable and graph that. The red lines shown in Figure 2
 286 depict the response surface for that variable with all other variables held at their mean values. Thus the red
 287 line in Figure 2a shows the variation in T_s as σ_1 varies with all other variables (σ_2 , σ_3 , $sHaz$, φ and δ) held at
 288 their mean values. There is a clear positive correlation of increasing T_s with increasing σ_1 , as expected from
 289 the definition of T_s and its underlying dependence on differential stress ($=\sigma_1 - \sigma_3$); the clear negative
 290 correlation of T_s with σ_3 shown in Figure 2c confirms this. Many of the response surface sections shown in
 291 Figure 2 are quasi-linear, but some are not: in particular, the dependencies of T_s on $sHaz$, strike and dip are
 292 all non-linear, and this further justifies the selection of a 2nd order quadratic response surface model.

293 A useful way to visualise the results from the response surface calculated by the MC simulation is the tornado
 294 plot shown in Figure 4c. Here the ranges of T_s for each input variable (shown as red lines over the histograms
 295 in Figure 2) are plotted to show the relative sensitivity of T_s to each variable. Variables are ranked from the
 296 largest range at the top to the lowest range at the bottom. Again, the core dependence of T_s on differential
 297 stress ($=\sigma_1 - \sigma_3$) is apparent, with σ_1 and σ_3 ranked highest in the plot. Interestingly, fault dip is ranked the
 298 next highest in terms of sensitivity and this reflects the geometry of this particular example. The Andersonian
 299 stress regime is for normal faulting, with σ_1 vertical. σ_2 is oriented parallel to fault strike ($sHaz = strike = 060$),
 300 and the fault dips at 60. This fault is therefore ideally oriented for slip in this stress field. Small changes to dip
 301 will influence the ratio of τ to σ_n , and therefore T_s .



302

303 **Figure 4.** Output from Monte Carlo simulation ($N_{MC}=5,000$) of slip tendency calculated using a quadratic
 304 response surface from synthetic input data. **a.** Histogram of calculated slip tendency values, in this case
 305 showing a quasi-normal distribution with a mode of ~ 0.55 . **b.** Cumulative distribution function (CDF) of
 306 calculated slip tendency values, showing the range in values from ~ 0.4 to ~ 0.7 . **c.** Tornado plot showing
 307 relative sensitivity to the input variables. The vertical dashed line shows the modal (most frequent) value of
 308 T_s from the MC ensemble.



309 **Figure 5.** Output from Monte Carlo sensitivity tests for slip tendency, T_s . **a.** Effect of variation in standard
 310 deviation of the least principal stress, σ_3 . **b.** Effect of variation in dispersion (κ parameter of the Von Mises
 311 distribution) of fault dip.
 312

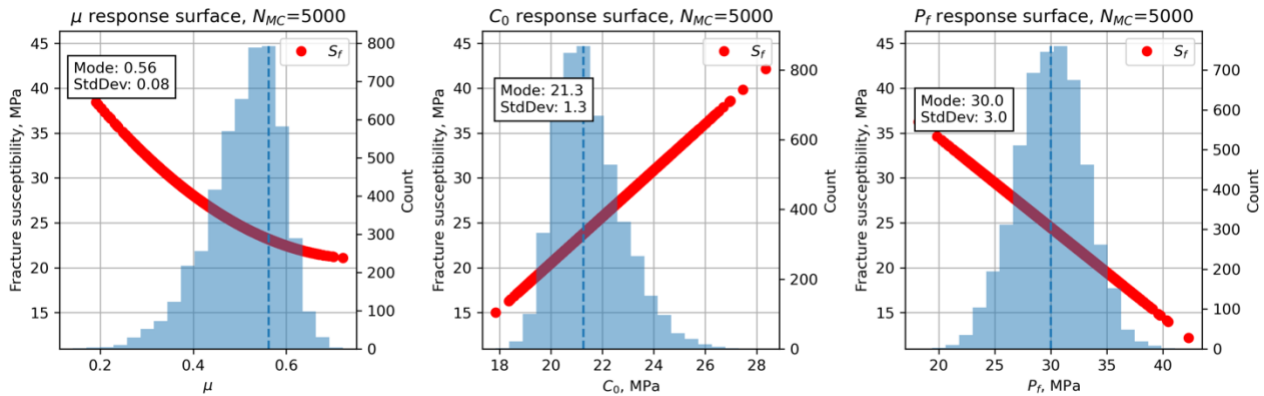
313 We can use a Monte Carlo approach to explore these sensitivities in more detail. Given the shape of the
 314 response surface sections shown in Figure 2 and the ranking of variables in Figure 4c, we can quantify how
 315 more or less variation in the inputs will affect the predicted T_s . Figure 5 shows the results of this sensitivity
 316 analysis for σ_3 and fault dip. The most significant effect on the CDF of T_s is produced by increasing the
 317 variation in σ_3 to 20% of the mean. This level of uncertainty for the minimum stress is not unreasonable in
 318 real-world scenarios (see Case Studies below). Increased uncertainty in σ_3 at this level leads to a $\sim 20\%$ chance
 319 of T_s being in excess of 0.7 ($p = 0.8$ for $T_s \leq 0.7$ from Figure 5a). Increased uncertainty in fault dip is achieved
 320 by varying the dispersion parameter κ of the Von Mises distribution (lower values of $\kappa =$ more dispersed).
 321 Very disperse distributions of fault dip with $\kappa = 20$ only change T_s by < 0.1 .

322 *Worked Example 2: synthetic Sf*

323 We can explore variations in predicted fracture susceptibility using the same principles as for slip tendency,
 324 but adjusted by incorporating three new variables as required by equation 3 – pore fluid pressure, friction
 325 coefficient and cohesion (code in GitHub: WorkedExample2.ipynb). The number of variables q is now 9, and
 326 therefore the design space used to compute the response surface is $3^q = 3^9 = 19,683$ data points. In practice
 327 this means a slower run-time, but still only takes a few minutes on a modern processor.

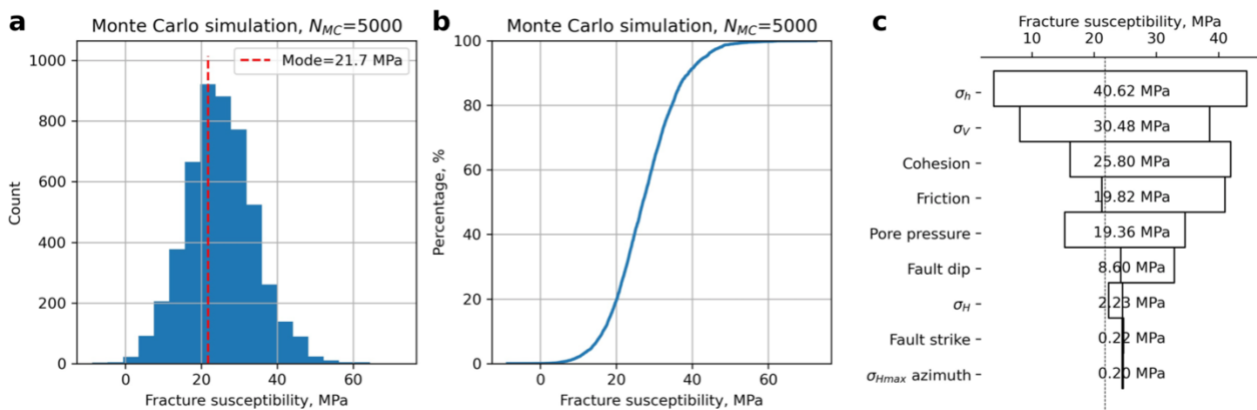
328 For this example, we use the same stress tensor as for the T_s example, with σ_1 as the maximum principal
 329 stress and vertical, i.e., an Andersonian normal fault regime for a depth of approximately 3 km. We constrain

330 the *in situ* pore pressure with a symmetrical normal distribution with a mean value of 30 MPa, which is
 331 approximately hydrostatic for a depth of 3 km, and with a variation of 10% of this mean. Friction is
 332 constrained by a skewed normal distribution with a mode of 0.56 and $\alpha = -3$, i.e., skewed towards lower
 333 values. This shape of distribution for friction coefficients is consistent with previous studies (e.g., Moos et al.,
 334 2003; Walsh & Zoback, 2016) but is open to question (see Discussion). Similarly for cohesion, we use a skewed
 335 normal distribution with a mode of 21 MPa and $\alpha = +3$, i.e., skewed towards higher values again consistent
 336 with previous work. These input variable distributions are documented in Table 2 (lower) and shown in the
 337 histograms of Figure 6.



338

339 **Figure 6.** Histograms of the input variables, in addition to those shown in Figure 2, used to calculate fracture
 340 susceptibility for the synthetic distributions shown in Table 2. Note the skewed (asymmetric) distributions
 341 for μ and C_0 .

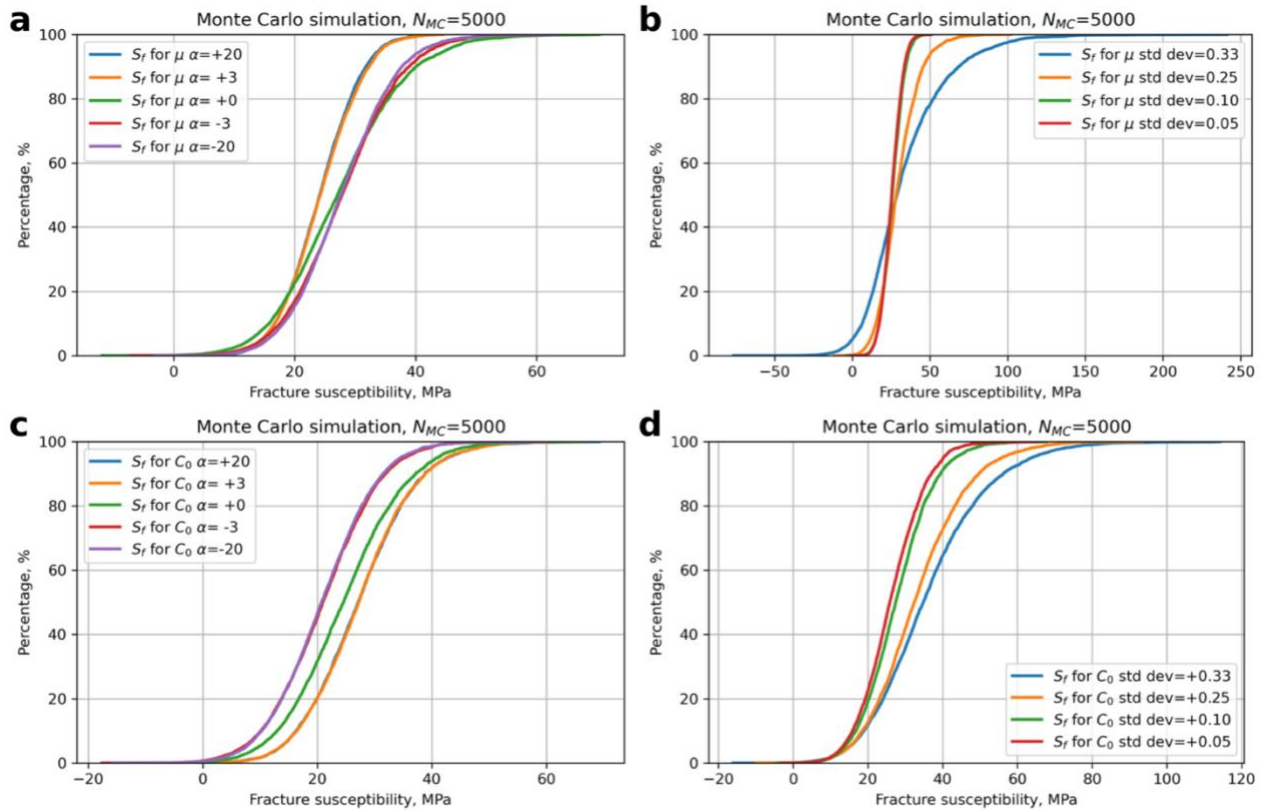


342

343 **Figure 7.** Output from Monte Carlo simulation ($N_{MC}=5,000$) of fracture susceptibility calculated using a
 344 quadratic response surface from synthetic input data. **a.** Histogram of calculated fracture susceptibility,
 345 showing a quasi-normal distribution with a mode of 21.7 MPa. **b.** Cumulative distribution function (CDF) of
 346 calculated fracture susceptibility, showing the range in values from just less than 0 to about 60 MPa. **c.**
 347 Tornado plot of relative sensitivities of the input variables used to calculate fracture susceptibility.

348 We calculate a quadratic response surface and use a Monte Carlo simulation ($N_{MC} = 5,000$) to generate the
 349 ensemble summarised in Figure 7. The mode of the distribution of S_f is 21.7 MPa meaning that, on average,
 350 an increase in pore fluid pressure of about 22 MPa above the average *in situ* value of 30 MPa is needed to
 351 push the effective stress state to Mohr-Coulomb failure. The histogram in Figure 7a is approximately
 352 symmetrical, perhaps with a slight skewness to higher values, and this is reflected in the CDF shown in Figure
 353 7b. The distribution is overwhelmingly positive, meaning that this fault is almost unconditionally stable for
 354 any change in pore fluid pressure, *at these conditions*. The response surface sections for μ , C_0 and P_f shown
 355 in Figure 6 (red lines) all show a strong influence on the fracture susceptibility, and these are confirmed in
 356 the tornado plot of Figure 7c. Pore fluid pressure exhibits a negative correlation with S_f (Figure 6c) which is
 357 consistent with the general principle of effective stress: i.e., if the original *in situ* pore pressure is already

358 high, it only takes a small perturbation (small $\Delta P_f = S_f$) to promote sliding failure. The response to changes in
 359 μ and C_0 is more interesting (Figure 6a and b). For this magnitude of cohesion, the effect of cohesion on S_f is
 360 greater than that of μ (C_0 ranks higher than μ in the tornado plot, Figure 7c), and the dependence of S_f on μ
 361 is negative. However, this relationship is not general as will be shown in the Case Study for the Porthtowan
 362 Fault Zone (see below).



363

364 **Figure 8.** Sensitivity of fracture susceptibility to variations in μ and C_0 . Note the changes in scale along the x-
 365 axis between the plots.

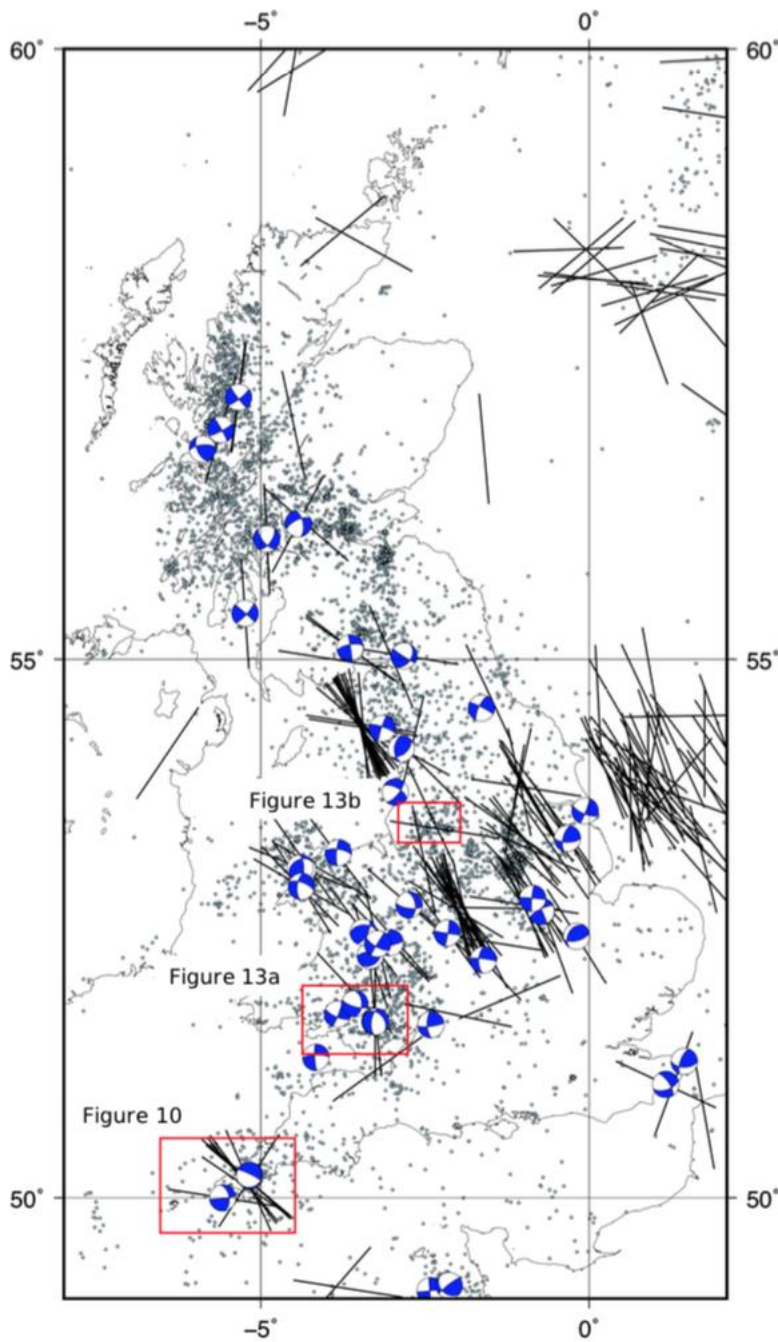
366 The relative asymmetries of the skewed normal distributions for μ and C_0 have already been noted. Given
 367 their significant effect on S_f (high ranking in the tornado plot, Figure 7c), it is useful to explore how the
 368 *skewness* of these distributions might influence S_f . Figure 8 shows the results of repeated Monte Carlo
 369 sensitivity tests for μ (Figure 8a, b) and C_0 (Figure 8c, d). For friction, a positive skewness to higher values (α
 370 > 0) would tend to reduce S_f – i.e., faults would be less stable. For cohesion, the opposite is true – a negative
 371 skewness ($\alpha < 0$) would make faults less stable to changes in P_f . These asymmetries are opposite to the ones
 372 used in the main Worked Example 2 and used by other workers (see Discussion). Widening the distributions
 373 for μ or C_0 by increasing their standard deviations (and retaining the original α values) tends to broaden the
 374 distribution of predicted S_f with asymmetry to higher (i.e., more stable) values.

375

376 Case Studies

377 The case studies have been chosen to illustrate how a combined RSM/MC approach can be used to estimate
 378 the probability of slip on one or more faults, and to show that even with relatively good – i.e., complete –
 379 input data, these predictions highlight that industrial operations remain significantly hazardous, with a
 380 greater than 1 in 3 chance of slip on many faults across different settings. Selected specific aspects of the
 381 modelling and the visualisation of results are emphasised in each case study. Figure 9 shows a map of the UK
 382 with the case study areas marked, together with the locations of instrumentally-recorded earthquakes and
 383 their focal mechanisms (Baptie, 2010). Also shown are data from the World Stress Map database of 2016
 384 (Heidbach et al., 2018) indicating the orientation of the maximum horizontal stress. A basic observation from
 385 this map is the level of complexity and heterogeneity in the present day seismotectonics of the UK, reflecting

386 the variation in the subsurface geology. However, there is a broad prevalence of NW-SE trending σ_{Hmax}
387 directions and strike-slip earthquake mechanisms.

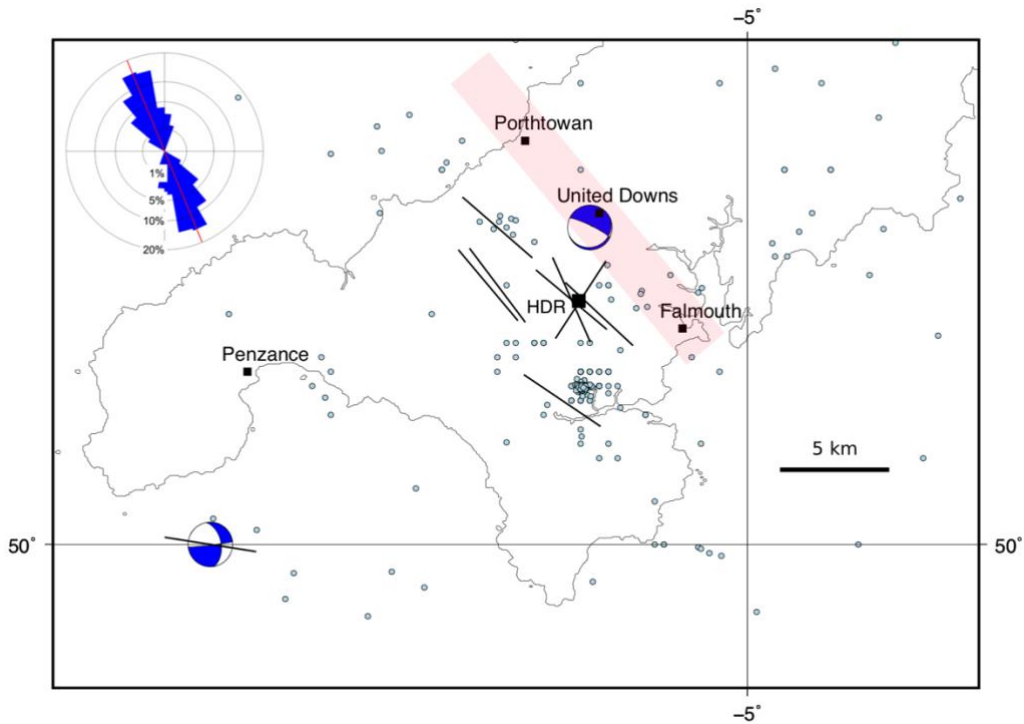


388
389 **Figure 9.** Map of most of the UK showing the locations of the selected case studies. Also shown: epicentres
390 of seismicity (light blue dots; BGS catalogue – Musson, 1996), focal mechanisms (blue and white; Baptie,
391 2010), and orientations of the maximum horizontal stress (black lines; World Stress Map data – Heidbach et
392 al., 2018).

393 *1. Porthtowan Fault Zone in Cornwall, UK*

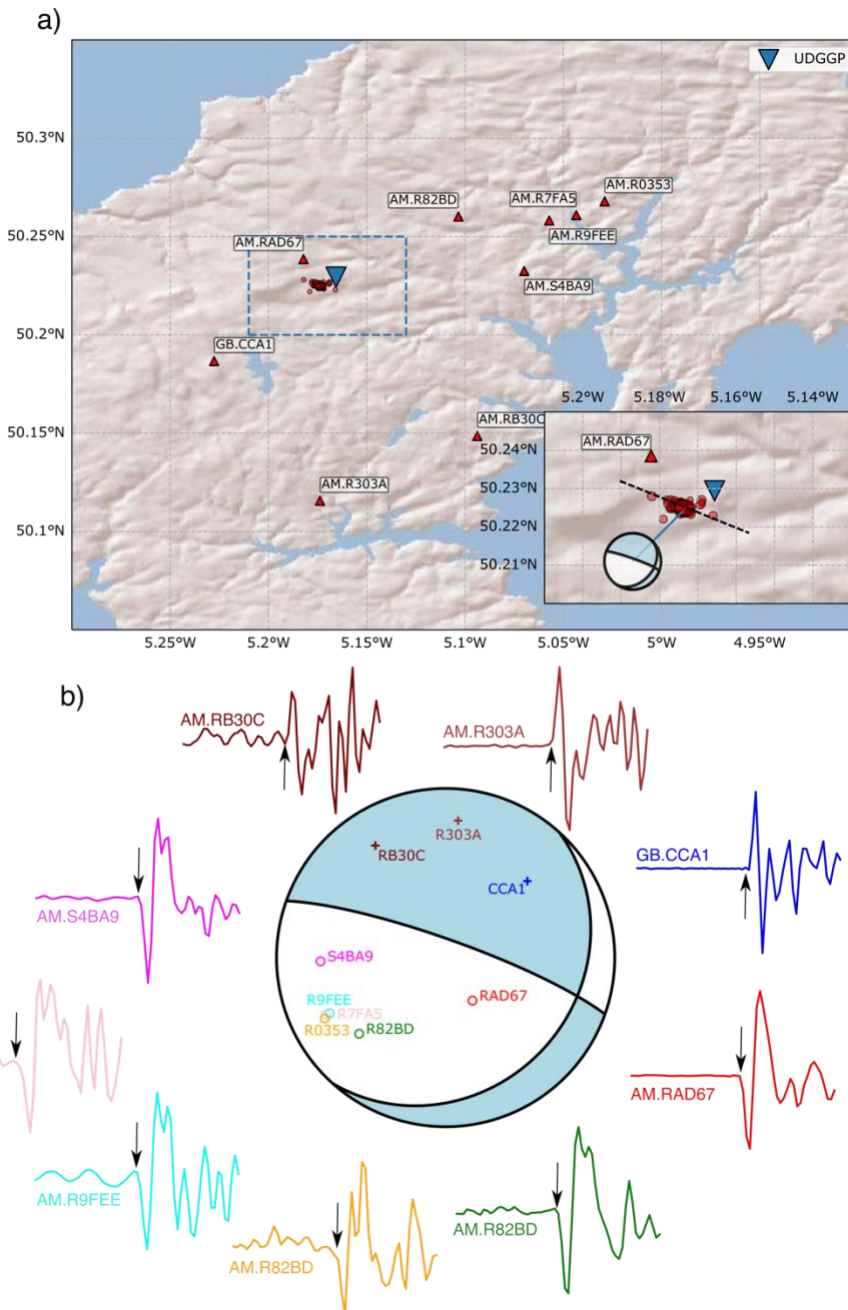
394 The Porthtowan Fault Zone (PFZ) cuts the Carnmenellis granite in Cornwall in southwest England (Figure 10).
395 This granite is a target for deep high-enthalpy geothermal energy due to its high radiogenic heat production
396 (Beamish & Busby, 2016). Following the Hot Dry Rock (HDR) project in the 1980s (Pine & Batchelor, 1984;
397 Batchelor & Pine, 1986), the United Downs pilot project has drilled two boreholes (UD-1, UD-2) to intersect
398 the fault zone at depths of about 5,275 m and 2,393 metres, respectively, making UD-1 the deepest onshore
399 borehole in the UK. The pilot project relies on shear-enhanced stimulation of pre-existing fractures (joints,

400 partially filled veins and faults) to drive fluid flow from the shallow injector (UD-2) to the deeper producer
 401 (UD-1). Temperatures at the base of UD-1 have been predicted at about 200°C (Ledingham et al., 2019).
 402 Shearing and downward flow of injected fluid was observed in boreholes as part of the earlier HDR project
 403 and tracked with measured microseismicity (Pine & Batchelor, 1984; Green et al., 1988; Li et al., 2018).



404
 405 **Figure 10.** Map of South West England showing: selected population centres, the United Downs deep
 406 geothermal pilot project and the former Hot Dry Rock project (black squares); epicentres of seismicity (light
 407 blue dots; BGS catalogue – Musson, 1996); focal mechanisms (blue and white; Baptie, 2010); and orientations
 408 of the maximum horizontal stress (black lines; World Stress Map data – Heidbach et al., 2018). Approximate
 409 trend and extent of the Porthtowan Fault Zone shown in pale red. Inset shows an equal area rose diagram
 410 with strikes of fault segments in the Porthtowan Fault Zone measured on BGS Falmouth sheet 352 ($N=140$;
 411 circular mean strike= 158° , circular standard deviation= 27°).

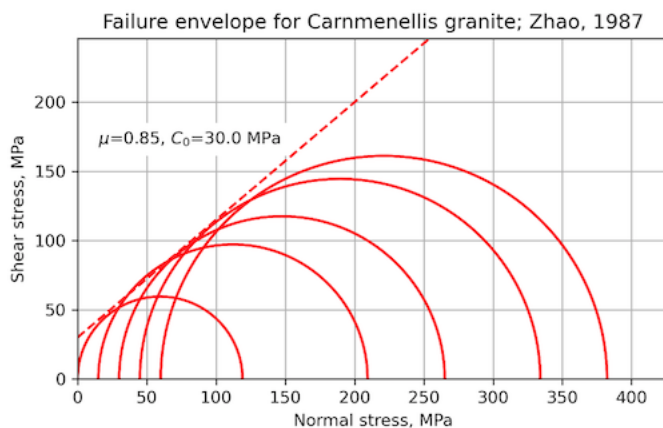
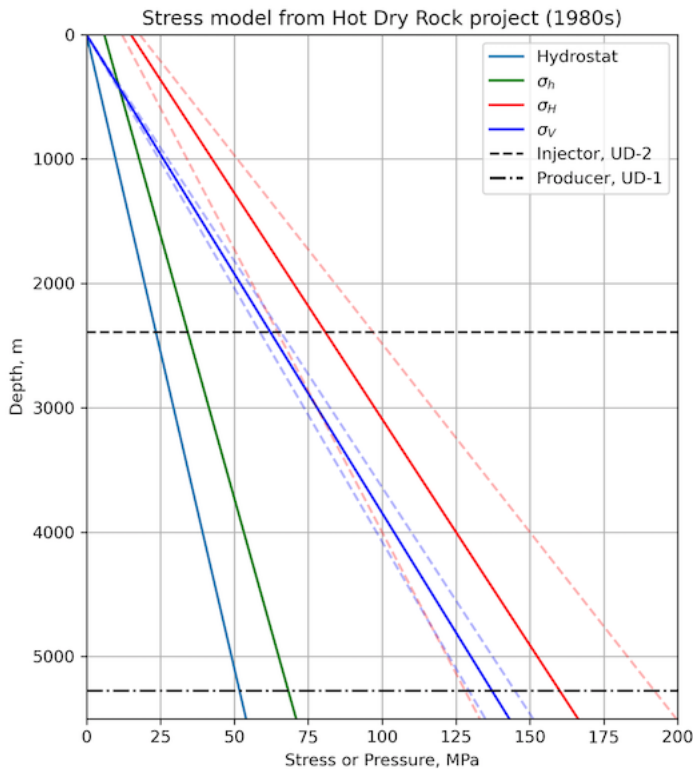
412 Figure 10 shows a map of SW England overlain with seismicity data from the BGS (Musson, 1996). The PFZ is
 413 poorly exposed inland, and runs NNW-SSE from Porthtowan on the north Cornish coast to Falmouth on the
 414 south coast (see inset rose diagram for strikes of constituent faults taken from the BGS Falmouth sheet 352).
 415 Overall, the fault zone is believed to dip steeply to the east at around 80° (Fellgett & Haslam, 2021). The
 416 azimuth of the maximum horizontal stress is broadly NW-SE, with one exception trending NE-SW.



417

418 **Figure 11. a.** Red triangles show Raspberry Shake (network code: AM) and BGS (network code: GB) seismic
 419 stations in Cornwall, with station names labelled. Seismicity during geothermal operations is indicated by red
 420 circles. The inset shows a close-up of the area demarcated by the blue dashed line in the main map. The black
 421 dashed line in the inset shows the broad WNW-ESE alignment in seismicity. **b.** Computed focal mechanism
 422 for the 2020-09-30 11:44:01 M_L 1.6 induced earthquake. First-motions are plotted on the focal sphere with
 423 “+” indicating positive polarity, and “o” for negative polarities. P-wave first-motions are plotted starting and
 424 ending 0.3 seconds before and after the picked arrival, respectively, and are coloured in the same way as the
 425 points on the focal sphere.

426



427

428 **Figure 12.** Constraints on input variables for the Porthtowan Fault Zone modelling. **a.** Stress-depth plot based
 429 on data and equations from the Hot Dry Rock project in the Carnmenellis granite (Batchelor & Pine, 1986).
 430 Also shown are the depths of the two wells in the pilot project at United Downs. **b.** Mohr diagram showing
 431 data from laboratory mechanical tests of Zhao (1987) for brittle failure of Carnmenellis granite at 200°C.
 432 Estimated Mohr-Coulomb failure envelope (dashed red line) is defined by $\mu=0.85$, $C_0=30$ MPa.

433 Detailed geomechanical analyses were performed in the Carnmenellis granite in the 1980s as part of the HDR
 434 project, and these provide useful constraints on the variation of stress and fluid pressure with depth (Figure
 435 12a; Batchelor & Pine, 1986). From these data, a strike-slip regime is most likely with $\sigma_1 = \sigma_{Hmax}$ and $\sigma_2 = \sigma_V$,
 436 but note the uncertainties (based on quoted values in Batchelor & Pine, 1986): from around the depth of the
 437 injector well at United Downs and deeper, a normal fault regime is also consistent with the data, i.e., $\sigma_1 = \sigma_V$
 438 and $\sigma_2 = \sigma_{Hmax}$. Note that the earlier HDR project did not target a specific fault zone in the granite.

439 The thermo-mechanical properties of the Carnmenellis granite have been studied by Zhao (1987). Figure 12b
 440 shows a Mohr diagram of data taken from Table 2.3 of Zhao (1987) for laboratory brittle failure tests
 441 conducted at 200°C (the approximate temperature of the injector well at United Downs). From these data,
 442 we have estimated a linear Mohr-Coulomb failure envelope defined by a friction coefficient of 0.85 and a

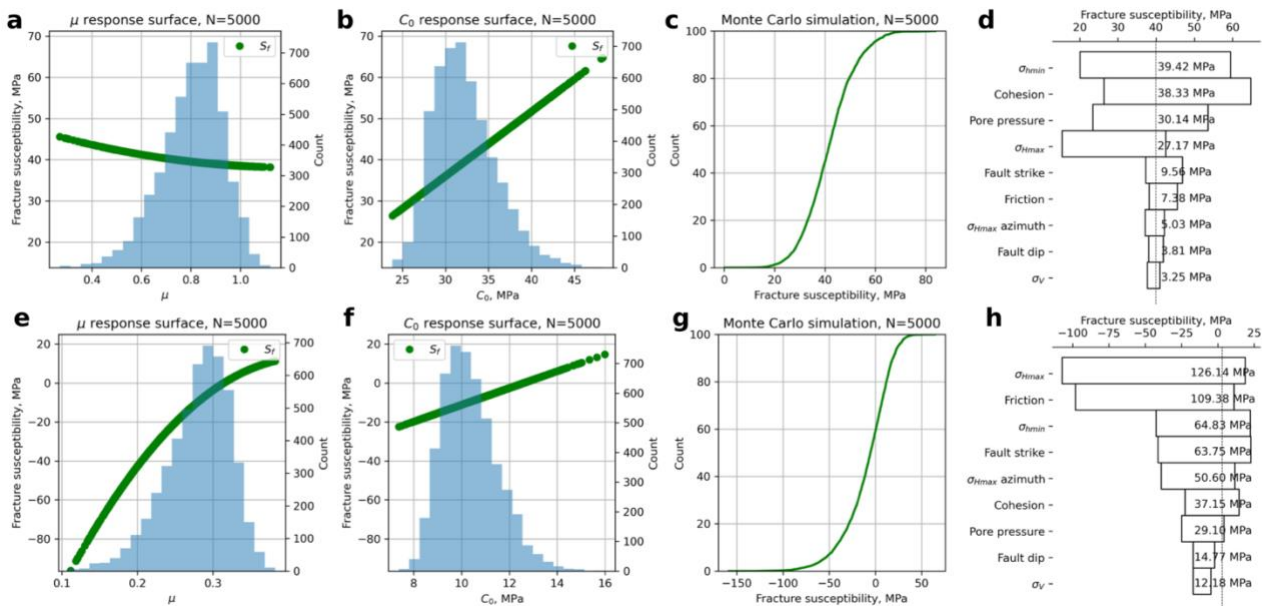
443 cohesive strength of 30 MPa. At the time of writing there are no published data for the mechanical properties
 444 of fault rocks sampled from the Porthtowan Fault Zone in the Carnmenellis granite.

445 We present model results for fracture susceptibility in the PFZ as the plan at United Downs (and elsewhere
 446 in the future) is to inject fluid into the fault zone in order to generate shear-enhanced permeability on pre-
 447 existing fractures. Table 3 lists the input variable distributions used in the “base case” model for hydrostatic
 448 pore fluid pressure in the fault zone and mechanical properties taken from laboratory tests of intact
 449 Carnmenellis granite (Figure 12b). The modelled depth is chosen as 4 km, in between the depths of the UD-
 450 1 and UD-2 wells.

Variable	Mean	Standard deviation (κ for Von Mises)	Units	Distribution	Comments
σ_v , vertical stress	105.0	5.25 (5% of mean)	MPa	Normal	Lithostatic for depth of 4 km, assuming average rock density of 2650 kg m ⁻³ Batchelor & Pine, 1986
σ_H , max. horizontal stress	125.0	25.0 (20% of mean)	MPa	Normal	Batchelor & Pine, 1986
σ_h , min. horizontal stress	53.0	5.3 (10% of mean)	MPa	Normal	Batchelor & Pine, 1986
P_f , pore fluid pressure	40.0	4.0 (10% of mean)	MPa	Normal	Hydrostatic for depth of 4 km, assuming average fluid density of 1000 kg m ⁻³
Azimuth of σ_{Hmax}	140	$\kappa=200$	°	Von Mises (circular Normal)	Batchelor & Pine, 1986
Fault strike	340	$\kappa=150$	°	As mapped	Digitised from BGS map
Fault dip	80.0	$\kappa=1000$	°	Von Mises (circular Normal), truncated at 0 and 90	
Friction, μ	0.85	0.17 (20% of mean)	n/a	Skewed normal	$\alpha = -3$ i.e., skewed low
Cohesion, C_0	30.0	6.0 (20% of mean)	MPa	Skewed normal	$\alpha = +3$ i.e., skewed high

451

452 **Table 3.** Distributions of input variables used in the base case model of fracture susceptibility in the
 453 Porthtowan Fault Zone.



454

455 **Figure 13.** Outputs from the Monte Carlo simulation of fracture susceptibility in the Porthtowan Fault Zone.
 456 **a-d.** The response surface for the base case, with friction and cohesion estimated from the laboratory failure
 457 tests of Zhao (1987), predicts positive fracture susceptibility i.e., a stable fault zone. The tornado plot (**d**)
 458 shows that for relatively high values of cohesion (mode of $C_0=30$ MPa in this case), the sensitivity to variations
 459 in friction is slight. **e-h.** In contrast, the response surface for the ‘weak fault’ case, with reduced values of
 460 friction and cohesion (mode of $\mu=0.3$, mode of $C_0=10$ MPa), predicts fault zone instability i.e., overwhelmingly
 461 negative values of S_f . The effect of friction on these predictions is now very strong, as shown in the shape of
 462 the response surface for μ (**e**) and in the ranking within the tornado plot (**h**).

463 The results from the Monte Carlo simulation of S_f for the PFZ are shown in Figure 13. For the base case, with
 464 hydrostatic pore fluid pressure and a ‘strong fault’ (mode of $\mu=0.85$, mode of $C_0=30$ MPa), the fault appears
 465 unconditionally stable for the modelled *in situ* stress variations. The CDF shows almost exclusively positive
 466 values of S_f up to about 60 MPa. Note that, for the input stress variations listed in Table 3, 22% of the MC
 467 simulations produced an Andersonian normal fault regime ($\sigma_1 = \sigma_v$), rather than a strike-slip ($\sigma_2 = \sigma_v$) regime.

468 232 microseismic events with hypocentre depths of 4-5 km were detected by the BGS during geothermal
 469 testing operations in 2021-2022 (http://www.earthquakes.bgs.ac.uk/data/data_archive.html; last accessed
 470 23 July 2021). The largest earthquake induced by geothermal operations during this period occurred on 2020-
 471 09-30 11:44:01, and had a local magnitude of M_L 1.6, and was felt by residents in the area. This event was
 472 well-recorded on a network of single-component Raspberry Shake stations (e.g. Holmgren & Werner, 2021)
 473 and a single station of the BGS permanent monitoring network (Figure 11a). These stations offer excellent
 474 azimuthal coverage of the geothermal seismicity, with the closest station lying only 2 km away (AM.RAD67).
 475 Since no focal mechanisms have yet been documented for these induced earthquakes, we used recorded P-
 476 wave first motions to compute a focal mechanism of the M_L 1.6 event using the method of Hardebeck &
 477 Shearer (2002). Take-off angles were computed using a 1D seismic velocity model for the Cornwall area
 478 (<http://earthwise.bgs.ac.uk/index.php/OR/18/015> Table 4: Depth/crustal velocity models used in eart
 479 hquake locations; last accessed 23 July 2021). The best-fitting focal mechanism (Figure 11b) indicates either
 480 normal faulting on a WNW-ESE steeply-dipping plane or strike-slip faulting on a shallow-dipping plane NE-
 481 SW striking plane. Single event relocated epicentres reported by the BGS, which use arrivals from a local
 482 dedicated microseismic monitoring array, show a NW-SE trend (Figure 11a), consistent with normal faulting
 483 on a steeply east-dipping, WNW-ESE striking plane during this earthquake. Negative P-wave polarities were
 484 recorded at AM.RAD67 for all $M > 0$ events, indicating that the same fault plane was reactivated during many
 485 of the induced events. The inferred fault plane is sub-parallel to the interpreted strike of the Porthtowan
 486 Fault Zone that is targeted by the geothermal testing. This observed normal faulting mechanism is consistent
 487 with our MC simulations (more than 1 in 5 of the predicted stress states were for normal faulting).

488

489 The response surface (green lines on Figure 13a-b) and the tornado plot of relative sensitivities of the input
490 variables (Figure 13d) shows a positive dependence of S_f on the cohesion, and that variations in friction are
491 relatively unimportant. If we reduce the strength of the modelled fault zone, by changing the input
492 distributions of μ and C_0 to lower values – but with the same shape and skewness – the situation changes.
493 The predicted fracture susceptibility is now much more strongly correlated with variations in friction, and
494 less so with variations in cohesion. This can be explained by looking at the underlying formula for S_f (equation
495 3), in particular the 2nd term on the RHS. If $C_0 > \tau$ then the numerator of this term can be negative, producing
496 a net positive term. However, if $C_0 < \tau$ and μ is small then this term is larger and negative. The important
497 point is that the probability distribution of S_f (compare Figure 13c and 13g) is controlled by the *relative*
498 magnitudes of μ and C_0 . In a weak fault zone, with low μ and low C_0 , the predictions are very sensitive to the
499 value of friction. In a strong fault, the effect of μ is less important. Thus, we need to know more about the
500 relationship between μ and C_0 in fault rocks (see Discussion).

501 2. Coalfields in South Wales and Greater Manchester, UK

502 Scope exists to extract low enthalpy geothermal heat from disused coalmines in the UK (Farr et al., 2016),
503 using either open- or closed-loop technology. Possible sites include the South Wales and Greater Manchester
504 coalfields, where folded and faulted Coal Measures of Westphalian (upper Carboniferous) age have been
505 mined for centuries, up until the 1980s. Initial plans for shallow mine geothermal schemes include *passive*
506 dewatering which may not change the loading on faults by much. However, *active* dewatering schemes can
507 promote ingress of deeper ground water (Farr et al., 2021), and as this fluid flow must be driven by gradients
508 in fluid pressure, this could in turn lead to the instability of faults at depth. The models below are for a depth
509 of 2 km.

510 The locations and orientations of faults have been taken from published BGS maps. For the South Wales
511 coalfield (Figure 14a), we used the BGS Hydrogeology map of S Wales to map the traces of faults in the Coal
512 Measures (Westphalian), and BGS 1:50k solid geology sheets over the same area to collect data on fault dips.
513 For the Greater Manchester coalfield (Figure 14b), we used the BGS 1:50k solid geology sheets for Wigan,
514 Manchester and Glossop. Faults were traced onto scanned images of the maps in a graphics package (Affinity
515 Designer on an Apple iPad using an Apple Pencil). These fault trace maps were saved in Scalable Vector
516 Graphics (.SVG) format, after deleting the original scanned image layer of the geological map. The saved .SVG
517 files were read into FracPaQ (Healy et al., 2017) to quantify their orientation distributions (inset rose plots in
518 Figure 14a and b). The fault trace maps were then overlain on maps containing historical seismicity and
519 available focal mechanisms (from the public BGS catalogue; Musson, 1996) and the orientations of σ_{Hmax}
520 taken from the World Stress Map project (Heidbach et al., 2018).

521 In the South Wales coalfield 3,408 fault segments were traced, and the dominant trend is clearly NNW/SSE,
522 but with important (and long) fault zones running ENE-WSW, such as the Neath and Swansea Valley
523 Disturbances (Figure 14a). From cross sections, we measured 142 fault dips to help constrain the distribution
524 of friction coefficients in these rocks (Figure 15b-c; see below), corrected for vertical exaggeration on the
525 section line where necessary. Focal mechanisms in this area ($n=4$) suggest that NNW/SSE and N/S faults are
526 active in the current stress regime. Historical seismicity is widely, if unevenly, distributed with no obvious
527 direct correlation to the surface mapped fault traces. For example, there are areas of intense surface faulting
528 but no recorded historical seismicity, and vice versa – areas with abundant historical events but few mapped
529 faults.

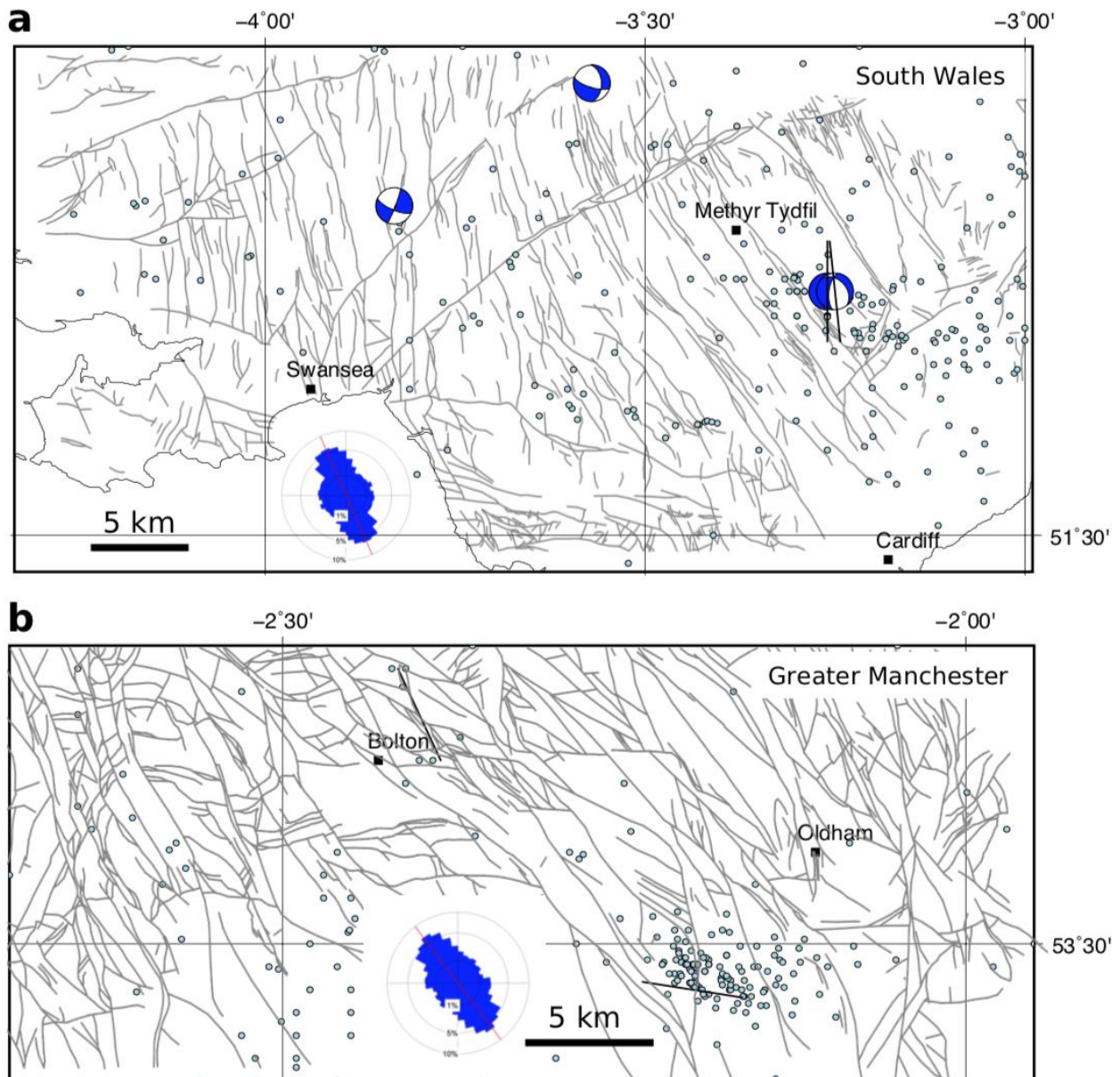
530 Around Greater Manchester 3,453 faults were traced, and the dominant trend is NW/SE, but E/W faults are
531 also present (Figure 14b). From cross sections, we measured 89 faults to help constrain the distribution of
532 friction coefficients in these rocks (Figure 15d-e; see below). Historical seismicity is again widely, if unevenly,
533 distributed with few obvious direct correlations to the surface mapped fault traces. However, there was an
534 earthquake swarm in 2002-2003 which comprised more than 100 events, with a maximum local magnitude
535 of 3.9. Calculated focal depths were 1 – 3 km, although these have large uncertainties (Walker et al., 2003).
536 The World Stress Map database has the orientation of σ_{Hmax} trending WNW/ESE in this area (Figure 12b).
537 These observations suggest that faults oriented more nearly E/W are more likely to slip in the current stress
538 regime.

539 There are no published geomechanical analyses for the variation of stress with depth for either of these two
540 areas. To constrain the depth dependence of stress, we have used larger scale syntheses of stress for onshore
541 UK produced by the BGS (e.g., Kingdon et al., 2016; Fellgett et al., 2018). The stress-depth plot in Figure 15a
542 has been constructed using the data shown in Fellgett et al. (2018), and shows that, in general, a strike-slip
543 fault regime with $\sigma_1 = \sigma_{Hmax}$ is most likely. However, given the known uncertainties in the data, a normal fault
544 regime ($\sigma_1 = \sigma_V$) cannot be ruled out, especially at depth. The azimuth of σ_{Hmax} is known to vary across the
545 UK ranging from ~130 to ~170 (Baptie et al., 2010; Becker & Davenport, 2001).

546 Despite the economic and historical significance of the Coal Measures, there are no published datasets of
547 laboratory measured friction or cohesion for either intact rocks or their faulted equivalents (although data
548 may exist in proprietary company records). Data for specific units of interest does exist, e.g., for the
549 Oughtibridge Ganister, a seat earth in the Coal Measures (Rutter & Hadizadeh, 1991); and the Pennant
550 Sandstone, a rare marine sandstone unit (Cuss et al., 2003; Hackston & Rutter, 2016), but a systematic
551 analysis of the volumetrically dominant sandstone, siltstone and mudstone formations is notably absent.
552 Instead, we use the measured dips of faults in the Coal Measures as a proxy for the coefficient of sliding
553 friction, using the relationship

554
$$\mu = 1/\tan(\pi - 2\beta)$$
 equation 14

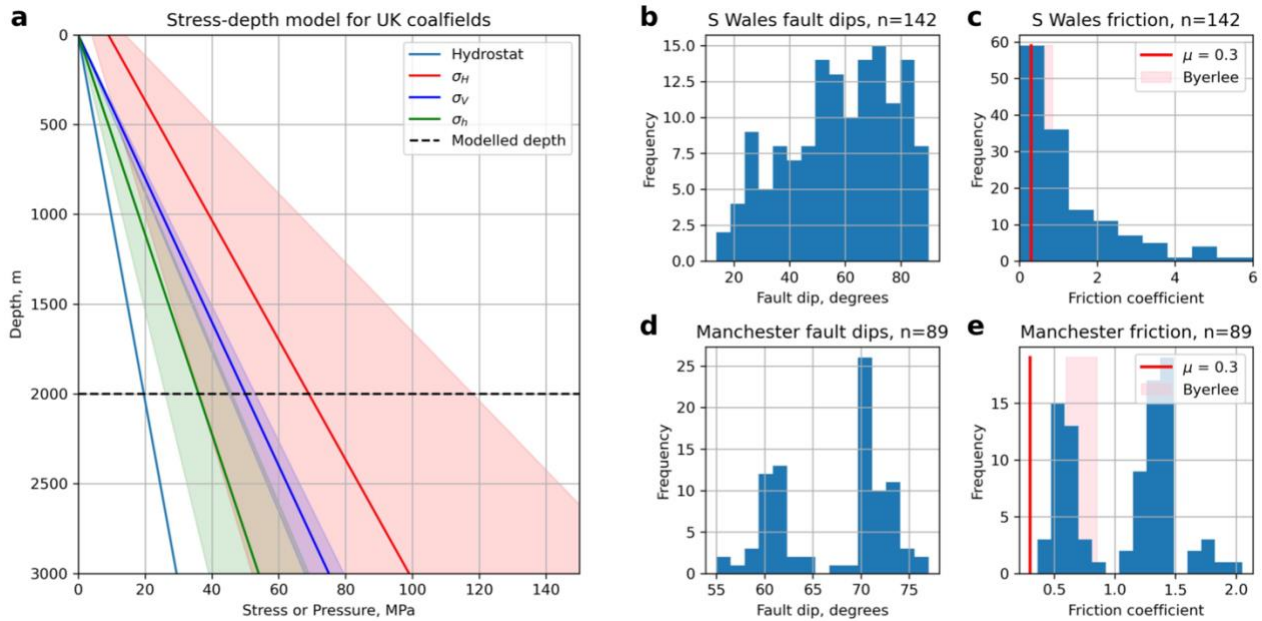
555 where β is the angle between the fault plane and σ_1 at failure (Jaeger et al., 2009; Carvell et al., 2014). Such
556 a calculation assumes Mohr-Coulomb failure and that the current dip of the fault is reasonably close to the
557 dip at failure in the post-Westphalian deformation of the coalfields. For measured fault dips $< 45^\circ$, we assume
558 that σ_1 was horizontal (Andersonian thrust/reverse fault regime) and for fault dips $\geq 45^\circ$ we assume σ_1 was
559 vertical (Andersonian normal fault regime). In practice, some of these faults probably originated as strike-slip
560 faults (i.e., with a sub-vertical dip and σ_2 vertical), and some of their dips have almost certainly been modified
561 by compaction since their formation. However, this method of estimating the likely range of friction
562 coefficients from measured dips remains simple to apply and useful to first order, in the absence of better
563 data. From the dip data, the calculated friction coefficients vary between 0.0 and 6.0 for South Wales, and
564 between 0.35 and 2.0 for Greater Manchester (Figures 15c and e, respectively).



565

566 **Figure 14.** Maps of selected UK coalfields (suggested sites of shallow mine geothermal energy) showing:
 567 selected population centres (black squares); epicentres of seismicity (light blue dots; BGS catalogue –
 568 Musson, 1996); focal mechanisms (blue and white; Baptie, 2010); and orientations of the maximum
 569 horizontal stress (black lines; World Stress Map data – Heidbach et al., 2018). Inset equal area rose diagrams
 570 show orientations of mapped faults. **a.** South Wales area. Faults in the Coal Measures taken from the BGS
 571 Hydrogeological Map of South Wales (1:125k) ($n=3,408$), with a circular mean strike= 156° and a circular
 572 standard deviation= 65° . **b.** Greater Manchester area. Faults in the Coal Measures taken from the BGS 1:50k
 573 sheets Wigan, Manchester and Glossop ($n=3,453$), with a circular mean strike= 143° and a circular standard
 574 deviation= 64° .

575 Based on the values of sliding friction calculated from measured fault dips across both coalfields a threshold
 576 stability value of $\mu=0.3$ is taken as a reasonable lower bound for faulted rock. This is the value used to
 577 compare with predicted slip tendencies calculated for each fault. For $T_s > 0.3$, the fault is deemed unstable,
 578 for $T_s \leq 0.3$ it is stable.



579

580 **Figure 15.** Constraints on input variables for the coalfield modelling of slip tendency. **a.** Stress-depth plot
 581 based on data from onshore UK (after Fellgett et al., 2018). Also shown is the modelled depth of 2 km. **b-e.**
 582 Histograms of fault dips measured cross-sections on published BGS 1:50k maps of South Wales and Greater
 583 Manchester, and calculated values of friction coefficients derived from these dips assuming Mohr-Coulomb
 584 failure. Byerlee friction ($\mu=0.6-0.85$) shown as shaded pink box. Modelled critical values of friction ($\mu=0.3$)
 585 shown by red lines.

586

Variable	Mean	Standard deviation (κ for Von Mises)	Units	Distribution	Comments
South Wales coalfield T_s model, depth=2 km					
σ_v , vertical stress	50.0	3.75 (5% of mean)	MPa	Normal	Lithostatic for depth of 2 km, assuming average rock density of 2500 kg m ⁻³
σ_H , max. horizontal stress	70.0	14.0 (20% of mean)	MPa	Normal	After Fellgett et al., 2018
σ_h , min. horizontal stress	35.0	3.5 (10% of mean)	MPa	Normal	After Fellgett et al., 2018
Azimuth of σ_{Hmax}	160	$\kappa=200$	°	Von Mises (circular Normal)	After Fellgett et al., 2018; Baptie, 2010; WSM, 2016
Fault strike	-	-	°	As mapped	Digitised from BGS Hydrogeology sheet
Fault dip	n/a	$\kappa=25$	°	Von Mises (circular Normal), truncated at 0 and 90	Fitted to data taken from cross-sections on BGS 1:50k sheets 229-231, 247-249, 263, 263
Greater Manchester coalfield T_s model, depth=2 km					
σ_v , vertical stress	50.0	7.5 (5% of mean)	MPa	Normal	Lithostatic for depth of 2 km, assuming average rock density of 2500 kg m ⁻³

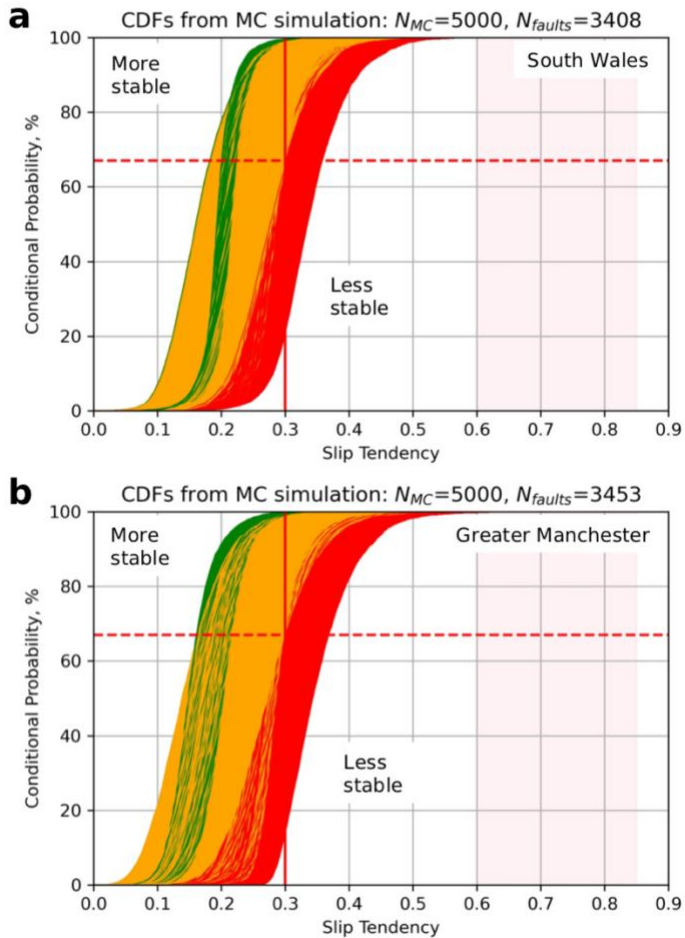
σ_H , max. horizontal stress	70.0	14.0 (20% of mean)	MPa	Normal	After Fellgett et al., 2018
σ_h , min. horizontal stress	35.0	3.5 (10% of mean)	MPa	Normal	After Fellgett et al., 2018
Azimuth of σ_{Hmax}	145	$\kappa=200$	°	Von Mises (circular Normal)	After Fellgett et al., 2018; Baptie, 2010; WSM, 2016
Fault strike	-	-	°	As mapped	Digitised from BGS 1:50k sheets 84-86
Fault dip	60.0	$\kappa=200$	°	Von Mises (circular Normal), truncated at 0 and 90	Fitted to data taken from cross sections on BGS 1:50k sheets 84-86

587

588 **Table 4.** Distributions of input variables used to model slip tendency in the coalfields of South Wales and
589 Greater Manchester.

590 Predictions of conditional probability for fault slip have been calculated for all faults in both coalfields using
591 slip tendency as the chosen measure: in the absence of detailed pore fluid pressure constraints or estimates
592 of cohesive strength, it is hard to justify modelling the fracture susceptibility. Slip tendency provides a first
593 order estimate of fault stability. A quadratic response surface was constructed for each coalfield using the
594 full range of measured fault strikes and dips, and the input variable distributions listed in Table 4 and
595 constrained by the data in Figure 15. Monte Carlo simulations ($N_{MC}=5,000$) were run for each mapped fault
596 segment with the other input variables drawn from their respective distributions. Note that the principal
597 stresses used were the same for both coalfields, for a depth of 2 km (see Table 4), but the azimuth of sH_{max}
598 was varied to reflect the regional differences reported by other authors (Becker & Davenport, 2001; Baptie,
599 2010), and the recorded focal mechanisms.

600 Output CDFs for all faults in both coalfields are shown in Figure 16. For South Wales ($N=3,408$ faults),
601 approximately 46% of faults are predicted to have a 1 in 3 chance of being unstable (i.e., $T_s > 0.3$, shown in
602 red), and 42% of faults are predicted to have a 1 in 10 chance of being unstable (shown in amber). For Greater
603 Manchester ($N=3,453$ faults), approximately 46% of faults are predicted to have a 1 in 3 chance of being
604 unstable (i.e., $T_s > 0.3$, shown in red), and 54% of faults are predicted to have a 1 in 10 chance of being
605 unstable (shown in amber).

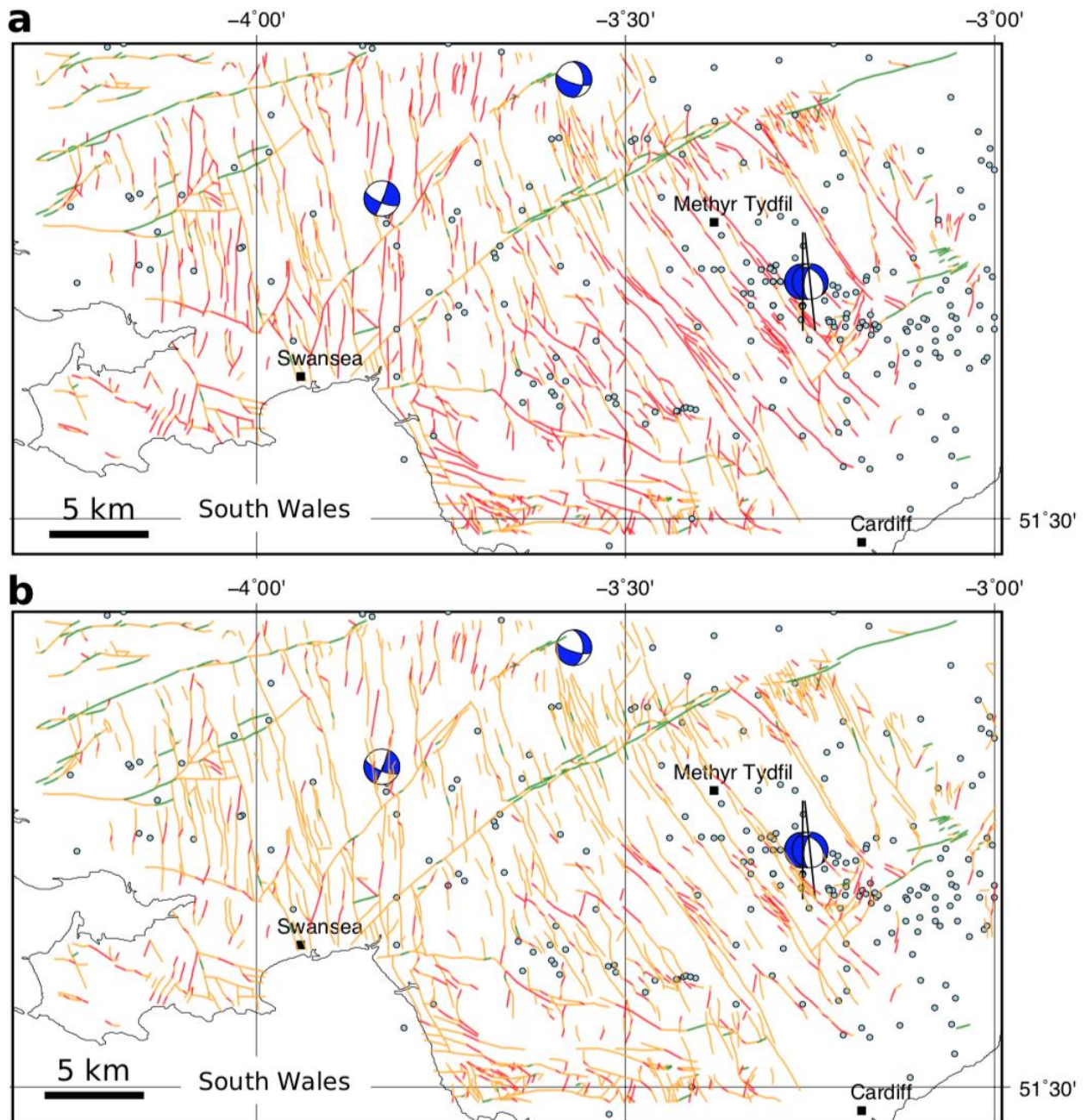


606

607 **Figure 16.** Output from the Monte Carlo modelling of slip tendency in UK coalfields. For slip tendency, more
 608 stable faults skew towards the left (low T_s), less stable faults skew to the right (high T_s). **a.** CDFs of predicted
 609 slip tendency for each mapped fault in South Wales. **b.** CDFs of predicted slip tendency for each mapped fault
 610 in Greater Manchester. Colour coding of CDFs – red: >33% chance of exceeding threshold friction ($\mu=0.3$,
 611 vertical red line), amber: >1% and <33% chance, green: < 1% chance. Range of Byerlee friction shown by pink
 612 shading.

613 The results from the RSM/MC modelling shown in the CDFs are replicated in map view in Figures 17 and 18.
 614 Each fault segment is colour coded using the same heuristic applied in the CDF: red faults have a conditional
 615 probability of at least 33% of their slip tendency exceeding the chosen threshold value of fault rock friction
 616 ($\mu=0.3$), amber (orange) faults have a 1-33% chance, and green faults have a less than 1% chance of being
 617 unstable.

618 For South Wales, the general pattern of the predictions is consistent with the recorded focal mechanisms
 619 (Figure 17a). The most likely fault segments to slip (coloured red) are those oriented either NNW/SSE or N/S,
 620 corresponding with one of the nodal planes in each of the focal mechanisms. Faults trending ENE/WSW, such
 621 as the Neath Disturbance, are predicted to have low probability of slip in the modelled stress regime (green).
 622 Note that the Swansea Valley Disturbance trends ENE/WSW as a fault zone, but the constituent fault
 623 segments are variously oriented including elements that trend NE/SW, and these are marked in red (high
 624 probability of slip). Blenkinsop et al. (1986) noted that this fault zone may in fact have a shallow dip at depth,
 625 which is not covered by the dip distribution used in our modelling, so further work is required here. The
 626 location with the most recorded events lies to the SE of Merthyr Tydfil, and this corresponds to an area with
 627 many mapped faults trending NW/SE marked with a high probability of slip, and consistent with two of the
 628 focal mechanisms.



629

630 **Figure 17.** Output from the Monte Carlo modelling of slip tendency in South Wales coalfield. **a.** Colour-coded
 631 fault map showing conditional probability of slip for each mapped fault. This map shows the unweighted
 632 values, as shown on the CDFs in Figure 14a. **b.** Colour-coded fault map showing conditional *weighted*
 633 probability of slip for each mapped fault. The weighted probability is calculated by multiplying the probability
 634 from the CDF in Figure 14a by the normalised fault smoothness, ranging from 1.0 for a perfectly straight (i.e.,
 635 smooth) fault, and tending to 0.0 for a rough fault. Colour coding of CDFs – red: >33% chance of exceeding
 636 threshold friction ($\mu=0.3$), amber: >1% and <33% chance, green: < 1% chance.

637

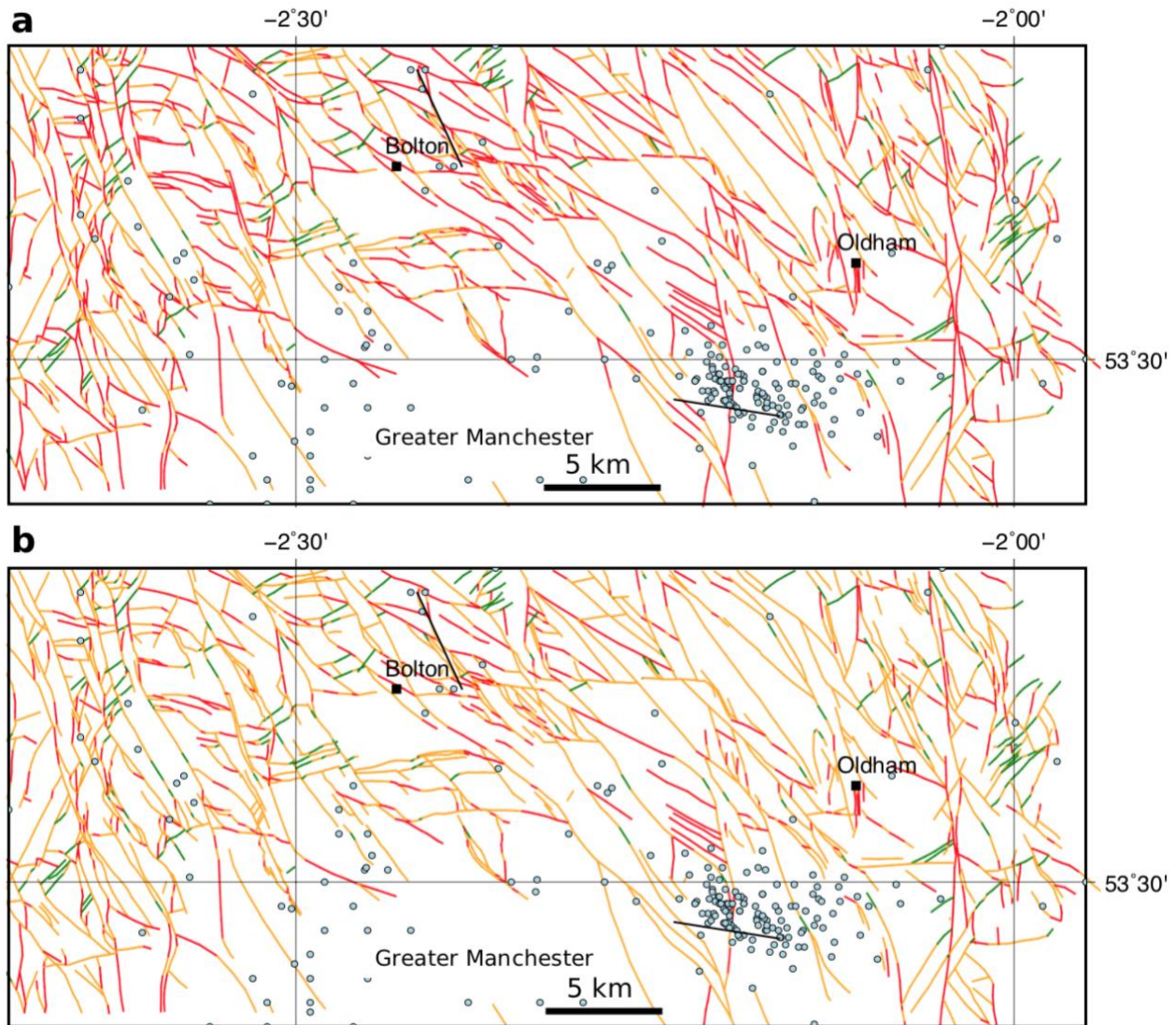
638

639

640

641

642 For Greater Manchester (Figure 18a), the simulation suggests that many faults are likely to slip in the
643 modelled stress regime, even though the recorded seismicity is generally sparse. The exception is the area of the 2002-2003 swarm near Manchester city centre. Here the recorded events coincide with mapped
644 surface faults trending WNW/ESE and predicted as likely to slip (red).
645



646
647 **Figure 18.** Output from the Monte Carlo modelling of slip tendency in Greater Manchester coalfield. **a.**
648 Colour-coded fault map showing conditional probability of slip for each mapped fault. This map shows the
649 unweighted values, as shown on the CDFs in Figure 14b. **b.** Colour-coded fault map showing conditional
650 *weighted* probability of slip for each mapped fault. The weighted probability is calculated by multiplying the
651 probability from the CDF in Figure 14b by the normalised fault smoothness, ranging from 1.0 for a perfectly
652 straight (i.e., smooth) fault, and tending to 0.0 for a rough fault. Colour coding of CDFs – red: >33% chance
653 of exceeding threshold friction ($\mu=0.3$), amber: >1% and <33% chance, green: < 1% chance.

654

655 Discussion

656 Stress, pressure, and temperature

657 The simulations described in this paper all critically depend on our knowledge of the *in situ* stress tensor. We
658 can constrain some of the components of this tensor better than others. The vertical stress (σ_v) is usually the
659 best constrained, a reflection of its derivation from the borehole density logs sampled at sub-metre
660 resolution. Our estimates of the horizontal stresses, σ_{Hmax} and σ_{Hmin} , remain poorly constrained. Even in cases

661 with relatively good data, e.g., from borehole leak-off tests (LOTs) and formation integrity tests (FITs), the
662 “data density” for these stress components is generally sparse (compared to σ_v), and we are stuck with
663 significant uncertainties. And these uncertainties matter, as shown by this study and previous work (e.g.,
664 Chiaramonte et al., 2008; Walsh & Zoback, 2016). The fundamental dependence of shear failure on
665 differential stress inherent in the Mohr-Coulomb failure criterion is reflected in the high ranking of stress
666 tensor components in the tornado plots shown in this study. Also, larger uncertainties in stress components
667 mean that the Andersonian regime may flip from the default “average” assumption to another orientation:
668 e.g., an apparently strike-slip regime may in fact include a significant proportion of normal fault possibilities
669 (>20% in the case of the Porthtowan Fault Zone shown here). One way to improve our knowledge of the
670 stress tensor, and especially the azimuth of σ_{Hmax} would be to exploit richer catalogues of seismicity to
671 produce more focal mechanisms for natural or induced events. Most countries would benefit from better –
672 i.e., more widespread and higher resolution – continuous seismic monitoring. While this may be expensive
673 with top of the range broadband equipment, citizen science devices, such as the Raspberry Shake, offer a
674 low cost and viable alternative (Cochran, 2018; Anthony et al., 2019; Hicks et al., 2021; Holmgren & Werner,
675 2021). Our study shows how Raspberry Shake data are effective for computing focal mechanisms. Analysis
676 of more events would allow stress inversions to be performed on the data measured by these devices,
677 especially when they are combined in *ad hoc* arrays to improve signal to noise ratios.

678 Pore fluid pressures at depth are also poorly known, even for a country like the UK with a long tradition of
679 geological (and geophysical) science and rich history of mining and drilling into the crust. Most importantly,
680 our knowledge of measured *in situ* pore fluid pressures in and around fault zones is generally poor.
681 Theoretical predictions and model simulations abound, but direct measurements of this key parameter are
682 almost non-existent. We need to know the actual limits of pore fluid pressures in fault zones, and their likely
683 spatial and temporal variation over a fault plane throughout the seismic cycle.

684 The work described in this paper has ignored the effects of temperature. However, thermoelastic stress may
685 be more important than poroelastic stress by a factor of 10 (Jacquey et al., 2015). In short, colder injected
686 water may increase the chance of slip on a given fault. In the UK, our knowledge of the subsurface
687 temperature field is increasing (Beamish & Busby, 2016; Farr et al., 2021), but we need more data, and again,
688 especially from faulted rocks.

689 *Faults*

690 An implicit assumption in all of the modelling performed in this paper (and many others) is that we know
691 something about the fault which may slip: i.e., we can only quantify risk on known faults. There will, in
692 general, be many more unmapped faults in the subsurface, and these may be the ones most likely to slip due
693 to a change in loading (of either *in situ* stress or fluid pressure). This is apparent in the maps for the coalfields
694 shown in this paper in terms of the relative lack of correspondence between the surface mapped fault traces
695 and the locations of recorded earthquakes. Some of this “mismatch” could be explained by the dip of the
696 faults measured at the surface, but not all. Moreover, there are areas of apparently intense surface faulting
697 and no recorded seismicity, and vice versa (recorded seismicity but no mapped surface faults). Some advance
698 could be made to address this problem with the recognition that each recorded seismic event documents a
699 fault plane, assuming that a double couple focal mechanism implies fault slip rather than dilation from dyke
700 emplacement or other mechanisms. And therefore the 3D position of each focal mechanism points to at least
701 part of a subsurface fault. The challenge then lies in mapping these seismic event fault planes into a viable
702 fault network. Better data (i.e., higher spatial resolution and extending to smaller event magnitudes) from
703 more dense arrays of seismometers would help with this task, as for the refinement of stress estimates noted
704 above.

705 *Rock properties*

706 The importance of good data on rock properties has been emphasised above, in the Worked Example for
707 fracture susceptibility and in the case study for the Porthtowan Fault Zone. In general, we need more and
708 better data on coefficients of friction and cohesive strength, especially for the target formations of
709 decarbonisation operations. Moreover, we need data for the intact *and* faulted rocks. We also need better
710 constrained correlations among rock properties. A widely used method in oil and gas is to derive estimates

711 of friction coefficient and UCS from wireline log datasets measuring porosity, slowness (velocity) or elasticity
712 e.g., Chang et al., 2006. However, as noted by these authors, the correlations are strictly valid only for the
713 specific formations tested in the laboratory, and even then, the uncertainties remain large. A further issue is
714 the tendency to average wireline log derived estimates over a depth interval, when for most sections of crust
715 this is the direction in which rock properties are expected to vary most rapidly. The Porthtowan Fault Zone
716 example above highlighted another issue: the relative impact of cohesion and friction on the predicted
717 stability depends on the magnitude of the cohesion in relation to the shear stress on the fault. For low
718 cohesion values, the constraints on friction become much more important. We need systematic
719 investigations of frictional behaviour at low cohesive strength. We need detailed systematic correlations
720 among rock properties, especially for faulted crystalline basement rocks.

721 Collecting more laboratory data is no panacea, evidenced by the well-aired concerns over how we up-scale
722 rock properties and behaviours from mm- and cm-sized samples to whole fault zones. But calibrations and
723 correlations from careful, systematic laboratory data remain the cornerstone of estimating the key *in situ*
724 values. An interesting new focus would be to explore the nature of the skewness in mechanical property
725 datasets: why should friction coefficients skew low, and cohesive strength skew high?

726 The utility of the Mohr-Coulomb criterion used in this paper is largely down to its mathematical simplicity,
727 i.e., linearity and only two parameters (friction and cohesion). Other criteria are perfectly viable and could
728 easily be added to the pfs Python code, but some other failure criteria lack a clear mapping between their
729 parameters and the mechanics of sliding on rock surfaces.

730 *Applicability of T_s , T_d and S_f for quantifying risk*

731 A valid question is to ask whether any of these widely used measures of fault stability are, in fact, useful in
732 practical terms at the scale of faults on maps. All three measures focus on the simplified mechanics of slip on
733 a specific fault plane, with a fixed orientation and with specific rock properties. But seismic hazard is not
734 isolated at the level of single fault planes. Faults occur in patterns or networks, more or less linked together.
735 Geometrical factors may be more important than the specifics of either the *in situ* stress or the rock
736 properties, at the scale of observation. The observational record shows that bigger fault zones are the sites
737 of bigger earthquakes, and they are also the locus of most displacement in a given network. Conversely,
738 smaller faults host smaller seismic events, and accrue less overall displacement (Walsh et al., 2001). To begin
739 to address this issue, we can weight the conditional probabilities of slip for a specific fault segment by a
740 dimensionless normalised factor derived from the total length of the fault: e.g., $w_{size} = l_s / l_t$ where l_s is fault
741 segment length and l_t is fault trace length. An alternative, but related idea, is that of the relationship between
742 fault smoothness (or inversely, roughness) and fault maturity, and therefore seismic hazard (Wesnousky et
743 al., 1988). The most seismically active faults are not only, or necessarily, the largest ones in their network,
744 but tend to be the smoothest or most connected, reflecting the coalescence of fault segments through time
745 and the removal of asperities through repeated slip events (Stirling et al., 1996). Therefore, we can weight
746 the conditional probabilities of slip by a dimensionless factor of smoothness: $w_{smooth} = l_{straight} / \sum(l_s)$, where
747 $l_{straight}$ is the straight line length between fault end points, which is 1.0 for a perfectly smooth fault with all
748 segments parallel and connected, and tends to 0.0 for rough, complex fault traces. Examples of the effect of
749 these smoothness weightings applied to the conditional probabilities are shown in Figures 17b and 18b for
750 the UK coalfield faults. The net effect is to reduce the number of most risky faults (shown in red) by about
751 half. These approaches are the subject of further work and testing.

752

753 **Summary**

754 In this paper, we have described and explained the Response Surface Methodology and shown how it can be
755 combined with a Monte Carlo approach to generate probabilistic estimates of fault stability using published
756 measures of slip tendency, dilation tendency and fracture susceptibility. Simulations show that a quadratic
757 response surface always generates a better fit to the input variables in comparison to a linear surface, at the
758 cost of larger matrices (more computer memory) and longer run times. Worked examples to calculate T_s and
759 S_f with synthetic input distributions show how the quadratic response surfaces vary for each input parameter.
760 For slip and dilation tendency, the primary dependence is (as expected) on the maximum differential stress,

761 and therefore the maximum and minimum principal stresses of the *in situ* stress tensor, with a lesser
762 dependence on the fault orientation. For fracture susceptibility, the situation is more complex: if cohesion is
763 relatively high, S_f is mainly dependent on the *in situ* stresses and cohesion. But if cohesion is low – quite likely
764 in fault zones – then the dependence of S_f on friction is much more significant. This is a key finding: the
765 relative sensitivity of the input variables on the response surface varies with the absolute value of the
766 variables.

767 Sensitivity tests were used to assess how the shapes of different input distributions affect the predictions of
768 fault stability. Varying the spread of symmetric (normal, Gaussian) distributions of input variables has a
769 significant effect on the predictions, and this mirrors the reality of uncertainties in, for example, the principal
770 stresses in a standard geomechanical analysis. As noted above, the vertical stress is often well constrained
771 and has a lower relative standard deviation (say, 5% of the mean) than either the maximum or minimum
772 horizontal stresses (typically 15-20% of their mean value). The shape and spread of skewed (asymmetric)
773 distributions of rock properties (friction and cohesion) is also important. The direction of skewness is
774 described by the sign of the parameter α for the skewed normal distributions used in this paper to model
775 variations in rock properties. Friction is modelled with a negative skewness towards lower values, whereas
776 cohesion is modelled with positive skewness towards higher values, but systematic laboratory data are
777 needed to verify these assumptions. This will require a statistically significant number of repeat tests for each
778 property on quasi-identical samples of the same rock.

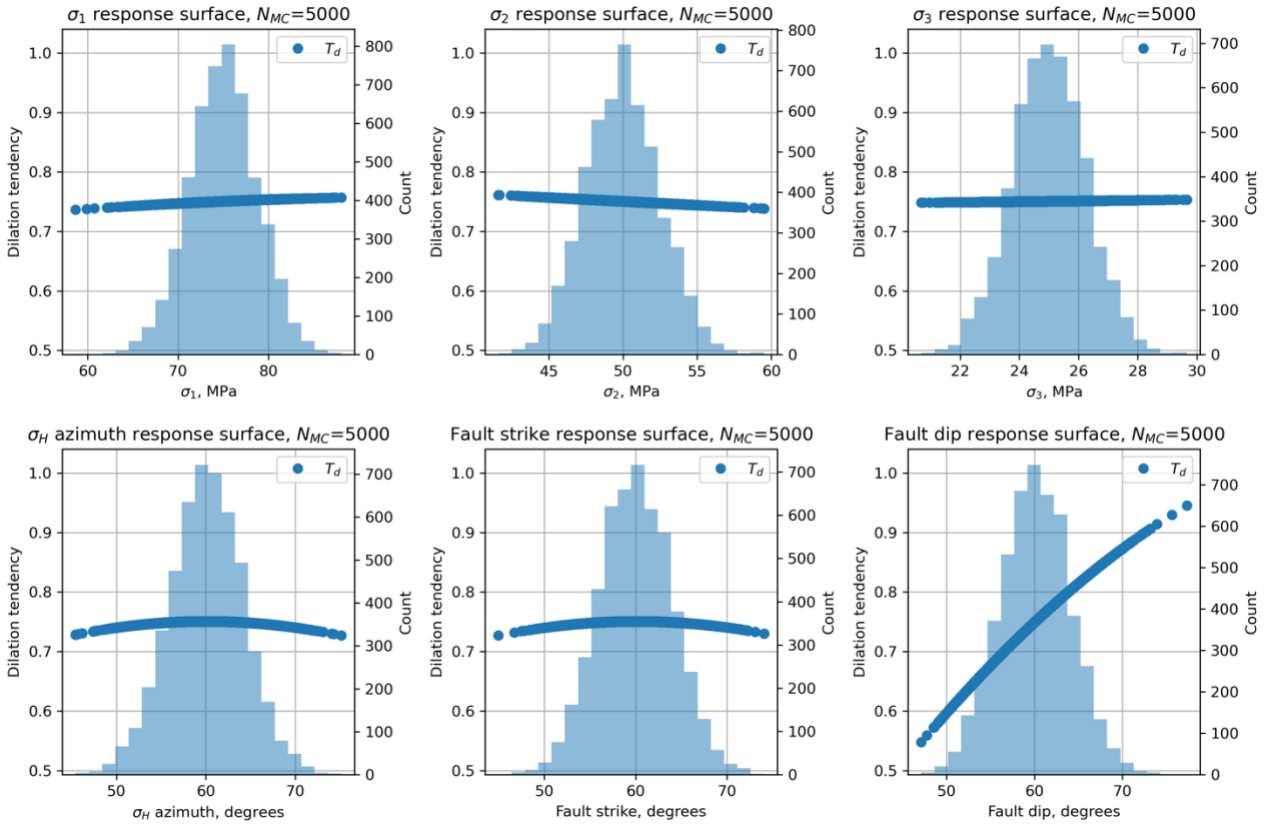
779 Case studies of three different locations demonstrated how a probabilistic approach can provide a useful
780 assessment of fault stability, including which of the input variables are the most important for a given
781 combination of *in situ* stress, fault plane orientation and rock properties. This then enables greater focus on
782 improving the estimates of the key variables, and the relationships between them. For the Porthtowan Fault
783 Zone in Cornwall, the modelling in this paper shows that we need more data for, and a better understanding
784 of the relationship between, coefficients of friction and cohesive strength, especially at low values of friction
785 (i.e., less than the Byerlee range of 0.6-0.85) to be expected in fault zones. For the coalfields in South Wales
786 and Greater Manchester, model outputs show how predictions of fault stability can be weighted by a simple
787 index of fault smoothness to begin to allow for the effects of geometrical weakening within the fault system
788 as whole, rather than focusing on each individual fault plane taken in isolation.

789 It's obvious that uncertainty in the input parameters must translate into uncertainty in the output
790 predictions. By combining a Response Surface Methodology with a Monte Carlo approach to the
791 quantification of fault stability, we can explore, understand, and quantify how differing degrees of
792 uncertainty among the input parameters feed through to uncertainty in the predicted stability measure.
793 Response surfaces and tornado plots can help to identify which parameters are the most important in a
794 particular analysis. Given our current state of knowledge of stress, fault orientations and fault rock
795 properties, probabilistic estimates and iterative modelling are useful approaches to begin to de-risk the
796 energy transition. Free, open source software to perform these analyses, such as the Python package pfs,
797 can help to encourage their wider adoption and further refinement ("given enough eyeballs, all bugs are
798 shallow"; Raymond, 2001). The deployment of abundant and relatively low-cost citizen science seismometers
799 (e.g., Raspberry Shakes) could synergise two critical issues: the wider involvement of the public into open
800 science debates about risk and the simultaneous collection of better data to constrain the local stress field.
801 The energy transition and decarbonisation are urgent and essential tasks: we will only be successful if we
802 manage to balance public perceptions of risk with the technical challenges inherent to the exploitation of
803 faulted rock.

804

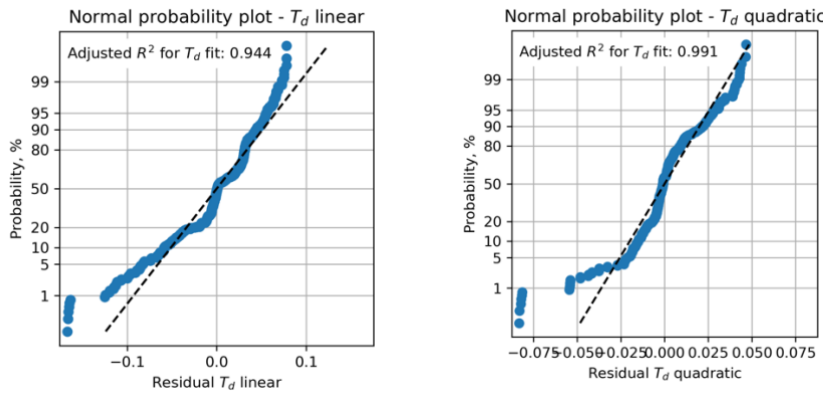
805 **Appendix A – Dilation tendency plots**

806 For completeness, we include the analysis of dilation tendency (T_d) for the same synthetic input dataset used
 807 to calculate slip tendency (T_s) – i.e., input variable distributions taken from Table 2.

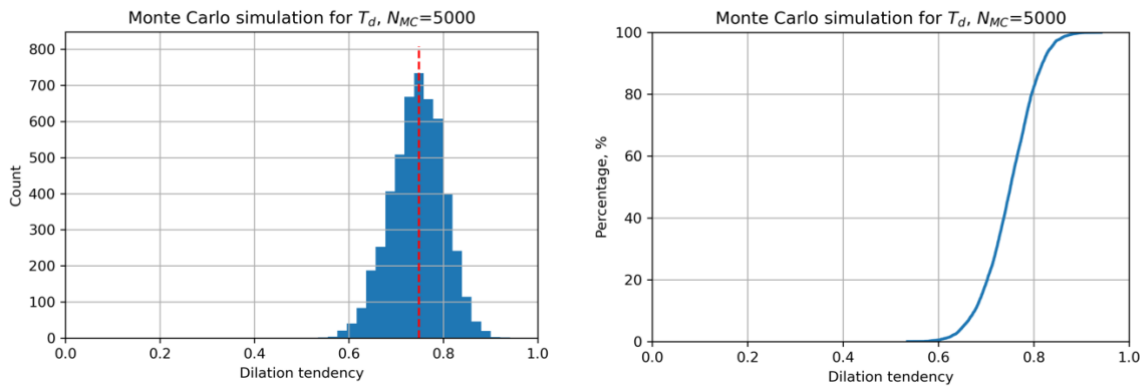


808

809 **Figure A1.** Histograms of input variables used to calculate dilation tendency T_d for the synthetic distributions
 810 shown in Table 2.



811 **Figure A2.** Residual plots for linear and quadratic response surfaces for dilation tendency using synthetic
 812 data. The quadratic fit has a higher value of the adjusted R^2 parameter and is therefore deemed better in this
 813 case.



814

815 **Figure A3.** Output from Monte Carlo simulation ($N_{MC}=5,000$) of dilation tendency calculated using a quadratic
 816 response surface from synthetic input data. **a.** Histogram of calculated dilation tendency values, in this case
 817 showing a quasi-normal distribution with a mode of ~ 0.75 . **b.** Cumulative distribution function (CDF) of
 818 calculated dilation tendency values, showing the range in values from ~ 0.5 to ~ 0.9 .

819

820 Code availability

821 <https://github.com/DaveHealy-github/pfs>

822

823 Data availability

824

825 Author contribution

826 DH – 80%, SH – 20%. DH originated the study, wrote the code, ran the models. SH contributed seismology
 827 data and expertise, and contributed to the writing of the text.

828

829 Competing interests

830 The authors declare that they have no conflicts of interest.

831

832 Acknowledgements

833 DH first presented the core ideas in this paper at the Tectonic Studies Group AGM in Cardiff in 2014, and
 834 enjoyed discussions there with Dr Jonathan Turner (RWM Ltd). Thanks to former PhD student Dr Sarah
 835 Weihmann (now at BGR) and co-supervisor Dr Frauke Schaeffer (Wintershall DEA) for discussions about using
 836 oil industry wireline log data for quantifying geomechanical models. GMT (Wessel et al., 2013) was used for
 837 the maps. SciPy (Virtanen et al., 2021), Numpy (Harris et al., 2020), and matplotlib (Hunter, 2007) were used
 838 for the Python pfs code and Allmendinger et al. (2012) for various geomechanical and geometrical algorithms.

839

840 References

841 Alcalde, J., Bond, C.E., Johnson, G., Ellis, J.F. and Butler, R.W., 2017. Impact of seismic image quality on fault
 842 interpretation uncertainty. GSA Today.

843 Allmendinger, R.W., Cardozo, N. and Fisher, D.M., 2011. Structural geology algorithms: Vectors and tensors.
 844 Cambridge University Press.

- 845 Anderson, E.M., 1905. The dynamics of faulting. *Transactions of the Edinburgh Geological Society*, 8(3),
846 pp.387-402.
- 847 Anthony, R.E., Ringler, A.T., Wilson, D.C. and Wolin, E., 2019. Do low-cost seismographs perform well enough
848 for your network? An overview of laboratory tests and field observations of the OSOP Raspberry Shake 4D.
849 *Seismological Research Letters*, 90(1), pp.219-228.
- 850 Ayash, S.C., Dobroskok, A.A., Sorensen, J.A., Wolfe, S.L., Steadman, E.N. and Harju, J.A., 2009. Probabilistic
851 approach to evaluating seismicity in CO₂ storage risk assessment. *Energy Procedia*, 1(1), pp.2487-2494.
- 852 Baptie, B., 2010. Seismogenesis and state of stress in the UK. *Tectonophysics*, 482(1-4), pp.150-159.
- 853 Barcelona, H., Yagupsky, D., Vigide, N. and Senger, M., 2019. Structural model and slip-dilation tendency
854 analysis at the Copahue geothermal system: inferences on the reservoir geometry. *Journal of Volcanology
855 and Geothermal Research*, 375, pp.18-31.
- 856 Batchelor, A.S. and Pine, R.J., 1986, August. The results of in situ stress determinations by seven methods to
857 depths of 2500 m in the Carnmenellis granite. In *ISRM International Symposium*. OnePetro.
- 858 Beamish, D. and Busby, J., 2016. The Cornubian geothermal province: heat production and flow in SW
859 England: estimates from boreholes and airborne gamma-ray measurements. *Geothermal Energy*, 4(1), pp.1-
860 25.
- 861 Becker, A. and Davenport, C.A., 2001. Contemporary in situ stress determinations at three sites in Scotland
862 and northern England. *Journal of Structural Geology*, 23(2-3), pp.407-419.
- 863 Blenkinsop, T.G., Long, R.E., Kuszniir, N.J. and Smith, M.J., 1986. Seismicity and tectonics in Wales. *Journal of
864 the Geological Society*, 143(2), pp.327-334.
- 865 Bond, C.E., 2015. Uncertainty in structural interpretation: Lessons to be learnt. *Journal of Structural Geology*,
866 74, pp.185-200.
- 867 Box, G.E., 1951. Wilson. KB [1951] On the Experimental Attainment of Optimum Conditions. *Journal of the
868 Royal Statistical Society, Series B (Methodological)*, 13(1), pp.1-45.
- 869 Carvell, J., Blenkinsop, T., Clarke, G. and Tonelli, M., 2014. Scaling, kinematics and evolution of a polymodal
870 fault system: Hail Creek Mine, NE Australia. *Tectonophysics*, 632, pp.138-150.
- 871 Chang, C., Zoback, M.D. and Khaksar, A., 2006. Empirical relations between rock strength and physical
872 properties in sedimentary rocks. *Journal of Petroleum Science and Engineering*, 51(3-4), pp.223-237.
- 873 Chiamonte, L., Zoback, M.D., Friedmann, J. and Stamp, V., 2008. Seal integrity and feasibility of CO₂
874 sequestration in the Teapot Dome EOR pilot: geomechanical site characterization. *Environmental Geology*,
875 54(8), pp.1667-1675.
- 876 Clarke, H., Verdon, J.P., Kettlely, T., Baird, A.F. and Kendall, J.M., 2019. Real-time imaging, forecasting, and
877 management of human-induced seismicity at Preston New Road, Lancashire, England. *Seismological
878 Research Letters*, 90(5), pp.1902-1915.
- 879 Cochran, E.S., 2018. To catch a quake. *Nature communications*, 9(1), pp.1-4.
- 880 CCC (UK Committee on Climate Change), 2019. Net Zero–Technical Report.
- 881 Cuss, R.J., Rutter, E.H. and Holloway, R.F., 2003. The application of critical state soil mechanics to the
882 mechanical behaviour of porous sandstones. *International Journal of Rock Mechanics and Mining Sciences*,
883 40(6), pp.847-862.
- 884 Das, D. and Mallik, J., 2020. Koyna earthquakes: a review of the mechanisms of reservoir-triggered seismicity
885 and slip tendency analysis of subsurface faults. *Acta Geophysica*, pp.1-16.

886 Elsworth, D., Spiers, C.J. and Niemeijer, A.R., 2016. Understanding induced seismicity. *Science*, 354(6318),
887 pp.1380-1381.

888 Farr, G., Sadasivam, S., Watson, I.A., Thomas, H.R. and Tucker, D., 2016. Low enthalpy heat recovery potential
889 from coal mine discharges in the South Wales Coalfield. *International Journal of Coal Geology*, 164, pp.92-
890 103.

891 Farr, G., Busby, J., Wyatt, L., Crooks, J., Schofield, D.I. and Holden, A., 2021. The temperature of Britain's
892 coalfields. *Quarterly Journal of Engineering Geology and Hydrogeology*, 54(3).

893 Fellgett, M.W., Kingdon, A., Williams, J.D. and Gent, C.M., 2018. Stress magnitudes across UK regions: New
894 analysis and legacy data across potentially prospective unconventional resource areas. *Marine and
895 Petroleum Geology*, 97, pp.24-31.

896 Fellgett, M.W. and Haslam, R., 2021, April. Fractures in Granite: Results from United Downs Deep Geothermal
897 well UD-1. In EGU General Assembly Conference Abstracts (pp. EGU21-5593).

898 Ferrill, D.A., Winterle, J., Wittmeyer, G., Sims, D., Colton, S., Armstrong, A. and Morris, A.P., 1999. Stressed
899 rock strains groundwater at Yucca Mountain, Nevada. *GSA Today*, 9(5), pp.1-8.

900 Goebel, T.H.W., Rosson, Z., Brodsky, E.E. and Walter, J.I., 2019. Aftershock deficiency of induced earthquake
901 sequences during rapid mitigation efforts in Oklahoma. *Earth and Planetary Science Letters*, 522, pp.135-143.

902 Green, A.S.P., Baria, R., Madge, A. and Jones, R., 1988. Fault-plane analysis of microseismicity induced by
903 fluid injections into granite. *Geological Society, London, Engineering Geology Special Publications*, 5(1),
904 pp.415-422.

905 Hackston, A. and Rutter, E., 2016. The Mohr–Coulomb criterion for intact rock strength and friction—a re-
906 evaluation and consideration of failure under polyaxial stresses. *Solid Earth*, 7(2), pp.493-508.

907 Hardebeck, J. L., & Shearer, P. M., 2002. A new method for determining first-motion focal
908 mechanisms. *Bulletin of the Seismological Society of America*, 92(6), 2264-2276.

909 Harris, C.R., Millman, K.J., van der Walt, S.J., Gommers, R., Virtanen, P., Cournapeau, D., Wieser, E., Taylor,
910 J., Berg, S., Smith, N.J. and Kern, R., 2020. Array programming with NumPy. *Nature*, 585(7825), pp.357-362.

911 Healy, D., Rizzo, R.E., Cornwell, D.G., Farrell, N.J., Watkins, H., Timms, N.E., Gomez-Rivas, E. and Smith, M.,
912 2017. FracPaQ: A MATLAB™ toolbox for the quantification of fracture patterns. *Journal of Structural Geology*,
913 95, pp.1-16.

914 Heidbach, O., Rajabi, M., Cui, X., Fuchs, K., Müller, B., Reinecker, J., Reiter, K., Tingay, M., Wenzel, F., Xie, F.
915 and Ziegler, M.O., 2018. The World Stress Map database release 2016: Crustal stress pattern across scales.
916 *Tectonophysics*, 744, pp.484-498.

917 Hennings, P.H., Lund Snee, J.E., Osmond, J.L., DeShon, H.R., Dommissie, R., Horne, E., Lemons, C. and Zoback,
918 M.D., 2019. Injection-induced seismicity and fault-slip potential in the Fort Worth Basin, Texas. *Bulletin of
919 the Seismological Society of America*, 109(5), pp.1615-1634.

920 Hicks, S. P., Verdon, J., Baptie, B., Luckett, R., Mildon, Z. K., & Gernon, T., 2019. A shallow earthquake swarm
921 close to hydrocarbon activities: Discriminating between natural and induced causes for the 2018–2019
922 Surrey, United Kingdom, earthquake sequence. *Seismological Research Letters*, 90(6), 2095-2110.

923 Hicks, S., Goes, S., Whittaker, A. C., & Stafford, P. J., 2021. Multivariate statistical appraisal of regional
924 susceptibility to induced seismicity: application to the Permian Basin, SW United States. *EarthArXiv*.
925 <https://doi.org/10.31223/X5NW3D>

926 Hincks, T., Aspinall, W., Cooke, R. and Gernon, T., 2018. Oklahoma's induced seismicity strongly linked to
927 wastewater injection depth. *Science*, 359(6381), pp.1251-1255.

- 928 Holmgren, J.M. and Werner, M.J., 2021. Raspberry Shake Instruments Provide Initial Ground-Motion
929 Assessment of the Induced Seismicity at the United Downs Deep Geothermal Power Project in Cornwall,
930 United Kingdom. *The Seismic Record*, 1(1), pp.27-34.
- 931 Hunter, J.D., 2007. Matplotlib: A 2D graphics environment. *Computing in science & engineering*, 9(03), pp.90-
932 95.
- 933 IPCC, 2018. *In: Masson-Delmotte, V., Zhai, P., Pörtner, H.O., Roberts, D., Skea, J., Shukla, P.R., Pirani, A.,
934 Moufouma-Okia, W., Péan, C., Pidcock, R. and Connors, S., 2018. Global warming of 1.5 C. An IPCC Special
935 Report on the impacts of global warming of, 1, pp.1-9.*
- 936 Jaeger, J.C., Cook, N.G. and Zimmerman, R., 2009. *Fundamentals of rock mechanics*. John Wiley & Sons.
- 937 Jacquey, A.B., Cacace, M., Blöcher, G. and Scheck-Wenderoth, M., 2015. Numerical investigation of
938 thermoelastic effects on fault slip tendency during injection and production of geothermal fluids. *Energy
939 Procedia*, 76, pp.311-320.
- 940 Kingdon, A., Fellgett, M.W. and Williams, J.D., 2016. Use of borehole imaging to improve understanding of
941 the in-situ stress orientation of Central and Northern England and its implications for unconventional
942 hydrocarbon resources. *Marine and Petroleum Geology*, 73, pp.1-20.
- 943 Ledingham, P., Cotton, L. and Law, R., 2019, February. The united downs deep geothermal power project. In
944 *Proceedings of the 44th Workshop on Geothermal Reservoir Engineering*, Stanford University, Stanford, CA,
945 USA (pp. 11-13).
- 946 Li, X., Main, I. and Jupe, A., 2018. Induced seismicity at the UK 'hot dry rock' test site for geothermal energy
947 production. *Geophysical Journal International*, 214(1), pp.331-344.
- 948 Lisle, R.J. and Srivastava, D.C., 2004. Test of the frictional reactivation theory for faults and validity of fault-
949 slip analysis. *Geology*, 32(7), pp.569-572.
- 950 McLennan, D., Noble, S., Noble, M., Plunkett, E., Wright, G. and Gutacker, N., 2019. *The English indices of
951 deprivation 2019: Technical report*.
- 952 Miocic, J.M., Johnson, G. and Bond, C.E., 2019. Uncertainty in fault seal parameters: implications for CO₂
953 column height retention and storage capacity in geological CO₂ storage projects. *Solid earth*, 10(3), pp.951-
954 967.
- 955 Moeck, I., Kwiatek, G. and Zimmermann, G., 2009. Slip tendency analysis, fault reactivation potential and
956 induced seismicity in a deep geothermal reservoir. *Journal of Structural Geology*, 31(10), pp.1174-1182.
- 957 Moos, D., Peska, P., Finkbeiner, T. and Zoback, M., 2003. Comprehensive wellbore stability analysis utilizing
958 quantitative risk assessment. *Journal of Petroleum Science and Engineering*, 38(3-4), pp.97-109.
- 959 Morris, A., Ferrill, D.A. and Henderson, D.B., 1996. Slip-tendency analysis and fault reactivation. *Geology*,
960 24(3), pp.275-278.
- 961 Musson, R.M., 1996. The seismicity of the British Isles. *Annals of Geophysics*, 39(3).
- 962 Myers, R.H., Montgomery, D.C. and Anderson-Cook, C.M., 2016. *Response surface methodology: process and
963 product optimization using designed experiments*. John Wiley & Sons.
- 964 Nolan, L., 2016, July. *The Welsh Index of Multiple Deprivation*. In *Presentation for the GSS Methodology
965 Conference (Vol. 6)*.
- 966 Pine, R.J. and Batchelor, A.S., 1984, October. Downward migration of shearing in jointed rock during hydraulic
967 injections. In *International Journal of Rock Mechanics and Mining Sciences & Geomechanics Abstracts (Vol.
968 21, No. 5, pp. 249-263)*. Pergamon.
- 969 Raymond, E., 2001. *The Cathedral & the Bazaar, Revised Edition*. O'Reilly.

970 Roberts, J. J., Bond, C. E., & Shipton, Z. K., 2021. Fracking bad language—hydraulic fracturing and earthquake
971 risks. *Geoscience Communication*, 4(2), 303-327.

972 Rohmer, J. and Bouc, O., 2010. A response surface methodology to address uncertainties in cap rock failure
973 assessment for CO₂ geological storage in deep aquifers. *International Journal of Greenhouse Gas Control*,
974 4(2), pp.198-208.

975 Rutter, E.H. and Hadizadeh, J., 1991. On the influence of porosity on the low-temperature brittle—ductile
976 transition in siliciclastic rocks. *Journal of Structural Geology*, 13(5), pp.609-614.

977 Sanchez Roa et al. Abstract

978 Stephenson, M.H., Ringrose, P., Geiger, S., Bridden, M. and Schofield, D., 2019. Geoscience and
979 decarbonization: current status and future directions. *Petroleum Geoscience*, 25(4), pp.501-508.

980 Stirling, M.W., Wesnousky, S.G. and Shimazaki, K., 1996. Fault trace complexity, cumulative slip, and the
981 shape of the magnitude-frequency distribution for strike-slip faults: A global survey. *Geophysical Journal
982 International*, 124(3), pp.833-868.

983 Streit, J.E. and Hillis, R.R., 2004. Estimating fault stability and sustainable fluid pressures for underground
984 storage of CO₂ in porous rock. *Energy*, 29(9-10), pp.1445-1456.

985 Townend, J. and Zoback, M.D., 2000. How faulting keeps the crust strong. *Geology*, 28(5), pp.399-402.

986 Verdon, J.P. and Budge, J., 2018. Examining the capability of statistical models to mitigate induced seismicity
987 during hydraulic fracturing of shale gas reservoirs. *Bulletin of the Seismological Society of America*, 108(2),
988 pp.690-701.

989 Virtanen, P., Gommers, R., Oliphant, T.E., Haberland, M., Reddy, T., Cournapeau, D., Burovski, E., Peterson,
990 P., Weckesser, W., Bright, J. and Van Der Walt, S.J., 2020. SciPy 1.0: fundamental algorithms for scientific
991 computing in Python. *Nature methods*, 17(3), pp.261-272.

992 Walker, A., Baptie, B. and Ottemoller, L., 2003. UK earthquake monitoring 2002/2003.

993 Walsh III, F.R. and Zoback, M.D., 2016. Probabilistic assessment of potential fault slip related to injection-
994 induced earthquakes: Application to north-central Oklahoma, USA. *Geology*, 44(12), pp.991-994.

995 Walsh, J.J., Childs, C., Meyer, V., Manzocchi, T., Imber, J., Nicol, A., Tuckwell, G., Bailey, W.R., Bonson, C.G.,
996 Watterson, J. and Nell, P.A., 2001. Geometric controls on the evolution of normal fault systems. *Geological
997 Society, London, Special Publications*, 186(1), pp.157-170.

998 Wang, Q., Ru, Z., Zhao, R., Yu, C., Liu, Y. and Deng, S., 2020. A study on permeability along strike slip faults in
999 Shunbei reservoir of Tarim Basin, China. *Energy Sources, Part A: Recovery, Utilization, and Environmental
1000 Effects*, pp.1-17.

1001 Wesnousky, S.G., 1988. Seismological and structural evolution of strike-slip faults. *Nature*, 335(6188), pp.340-
1002 343.

1003 Wessel, P., Smith, W.H., Scharroo, R., Luis, J. and Wobbe, F., 2013. Generic mapping tools: improved version
1004 released. *Eos, Transactions American Geophysical Union*, 94(45), pp.409-410.

1005 Williams, J.D., Fellgett, M.W. and Quinn, M.F., 2016. Carbon dioxide storage in the Captain Sandstone aquifer:
1006 determination of in situ stresses and fault-stability analysis. *Petroleum Geoscience*, 22(3), pp.211-222.

1007 Williams, J.D.O., Gent, C.M.A., Fellgett, M.W. and Gamboa, D., 2018. Impact of in situ stress and fault
1008 reactivation on seal integrity in the East Irish Sea Basin, UK. *Marine and Petroleum Geology*, 92, pp.685-696.

1009 Zhao, J., 1987. Experimental studies of the hydro-thermo-mechanical behaviour of joints in granite. Unpubl.
1010 PhD thesis, Imperial College, London, UK.

1011